Frontogenesis in the Agulhas Return Current Region Simulated by a High-Resolution CGCM

Shun Ohishi[a] and Tomoki Tozuka

Department of Earth and Planetary Science, Graduate School of Science, University of Tokyo, Tokyo, Japan

Meghan F. Cronin

NOAA/Pacific Marine Environmental Laboratory, Seattle, Washington

(Manuscript received 24 February 2017, in final form 30 June 2017)

ABSTRACT

Detailed mechanisms for frontogenesis/frontolysis of the sea surface temperature (SST) front in the Agulhas Return Current (ARC) region are investigated using outputs from a high-resolution coupled general circulation model. The SST front is maintained throughout the year through an approximate balance between frontolysis by surface heat flux and frontogenesis by horizontal advection. Although a southward (northward) cross-isotherm flow on the northern (southern) side of the front is weaker than a strong eastward along-isotherm current in the frontal region, this cross-isotherm confluent flow advects warmer (cooler) temperature toward the SST front north (south) of the front and acts as the dominant frontogenesis mechanism. In addition, stronger (weaker) frontogenesis in austral summer (winter) is attributed to the stronger (weaker) cross-isotherm confluence, which may be linked to seasonal variations of the Agulhas Current, ARC, and Antarctic Circumpolar Current. On the other hand, the contribution from entrainment is relatively small, because frontolysis by larger (smaller) entrainment velocity on the northern (southern) side opposes frontogenesis by less (more) effective cooling associated with a thicker (thinner) mixed layer and smaller (larger) temperature difference between the mixed layer and entrained water in the northern (southern) region. To gain further insight into the time-mean cross-isotherm confluent flow in the frontal region, the vorticity balance is examined. It is shown that anticyclonic (cyclonic) vorticity advection north (south) of the front by the mean cross-isotherm confluence is in balance with the sum of cyclonic (anticyclonic) vorticity advection by the mean along-isotherm flow and cross-isotherm eddy–mean interaction.

1. Introduction

In midlatitudes, it has long been accepted that atmospheric forcing causes sea surface temperature (SST) variations, and oceanic effects on the atmosphere are negligible (e.g., Frankignoul 1985; Kushnir et al. 2002). However, recent satellite and in situ observations (e.g., Tokinaga et al. 2009; Cronin et al. 2010) and high-resolution numerical models (e.g., Nonaka et al. 2009) revealed substantial impacts of SST fronts on the overlying atmosphere in western boundary currents and their extension regions: the Kuroshio and its extension, Gulf Stream (e.g., Kelly et al. 2010; Kwon et al. 2010), Brazil–

Malvinas Confluence (e.g., Tokinaga et al. 2005), and Agulhas Return Current (ARC; e.g., O'Neill et al. 2005) region. In particular, SST fronts have been shown to influence the atmosphere through their impacts on the static stability (e.g., Nonaka and Xie 2003), pressure fields (e.g., Minobe et al. 2008, 2010), and atmospheric baroclinicity (e.g., Nakamura et al. 2008; Ogawa et al. 2012). Although the importance of SST fronts associated with western boundary currents and their extensions has been recognized, past studies did not investigate reinforcement and relaxation processes for the SST fronts, that is, frontogenesis and frontolysis, in a quantitative manner.

Recently, using observational datasets and outputs from a high-resolution coupled general circulation model (CGCM), Tozuka and Cronin (2014) and Ohishi et al. (2016) quantitatively investigated frontogenesis/frontolysis in the ARC region in the southwestern Indian Ocean, where the monsoonal wind influences are

---

[a] Current affiliation: Institute for Space-Earth Environmental Research, Nagoya University, Nagoya, Japan.

Corresponding author: Shun Ohishi, ohishi@isee.nagoya-u.ac.jp

relatively weak and air–sea interaction associated with the SST front can be detected more easily (Fig. 1). The Agulhas Current flows southward along the east coast of the African continent and retroflects south of South Africa (Fig. 1a). Thereafter, the ARC flows eastward and merges with the Antarctic Circumpolar Current (ACC) around 45°–40°S, 40°E (Lutjeharms and Ansorge 2001; Boebel et al. 2003; Lutjeharms 2006; Beal et al. 2011). Throughout the year, a sharp SST front is found in the ARC region (Fig. 1b; Nakamura and Shimpo 2004), which is maintained through a balance between the frontolysis by surface net heat flux (NHF) and frontogenesis by oceanic processes (Tozuka and Cronin 2014; Ohishi et al. 2016). Furthermore, these authors pointed out how mixed layer processes can change the effective heat capacity of the mixed layer and thereby affect the frontogenesis/ frontolysis associated with surface heat fluxes. Through temporal and spatial variations in the mixed layer depth (MLD), the NHF strongly (weakly) relaxes the SST front in austral summer (winter). On the other hand, Ohishi et al. (2016) estimated frontogenesis by oceanic processes as a residual in observation and simulation because of the insufficient number of velocity observations and low skill in simulating the ocean interior field, respectively.

Past studies of frontogenesis are mostly based on idealized models. For example, the seminal studies of atmospheric frontogenesis by Hoskins (1971) and Hoskins and Bretherton (1972) used idealized models that incorporated a horizontally barotropic confluent flow. MacVean and Woods (1980) and Thompson (2000) then extended this to oceanic fronts. Rudnick and Davis (1988) proposed the solution of an initial-value problem whereby a front is developed with time by a confluent flow. These models, with confluent flow, were able to simulate an instantaneous front, but a discontinuity and divergence tended to form in a finite time because of the absence of frontolysis processes to balance with the frontogenesis.

Later, idealized models that incorporated baroclinic instability dynamics were used in the frontogenesis studies (e.g., Samelson 1993; Samelson and Chapman 1995; Spall 1995; Wang 1993). These studies were motivated by an intensive aircraft, ship, and mooring observational study in a frontal region of the western North Atlantic in 1984–86 called Frontal Air–Sea Interaction Experiment (FASINEX; Weller 1991; Pollard and Regier 1992). They demonstrated that frontogenesis occurs because of eddies and baroclinic waves through energy conversion from potential energy to eddy kinetic energy. More recently, Waterman and Jayne (2011) and Waterman and Hoskins (2013) analyzed frontogenesis by applying a flow with potential to cause barotropic instability to the western boundary in idealized models.
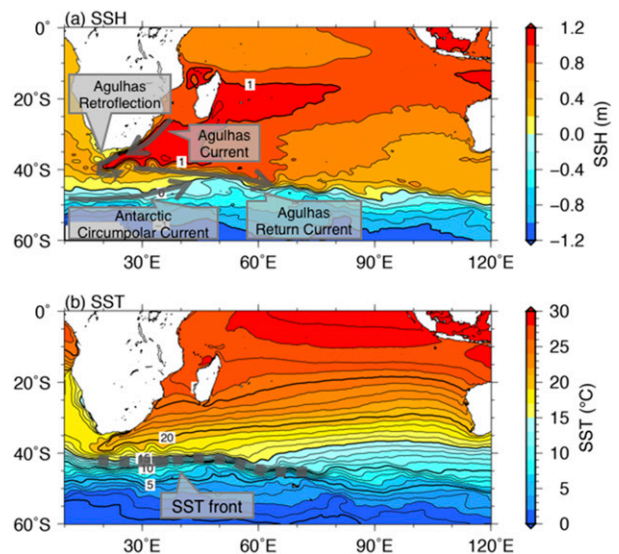

FIG. 1. Observed climatological mean (a) SSH and (b) SST. Thin (thick) contour intervals are 0.2 (1) m in (a) and 1 (5) °C in (b). In (a), the gray arrows indicate the Agulhas Current, Agulhas Retroflection, ARC, and ACC. In (b), the gray dotted line represents the SST front position.

Reproducing a time-mean jet and a pair of counterrotating recirculation gyres at the flank of the jet, they suggested that eddies have roles in driving the mean jet and recirculation through influences on the speed and direction of the mean velocity (Hoskins 1983; Cronin 1996).

While oceanic frontogenesis has been mostly investigated with idealized models, these types of simplified models lack realistic factors such as atmospheric forcing and ocean interior structure. For the above reason, in this study, detailed mechanisms of frontogenesis by oceanic processes in the ARC region are investigated using outputs from a high-resolution CGCM with good skill in simulating the ocean interior field.

This paper is organized as follows. A brief description of a high-resolution CGCM, observational datasets, and methods is provided in the next section. In section 3, characteristics of the simulated SST front and MLD in the ARC region are verified, and detailed mechanisms of frontogenesis/frontolysis in the ARC region are investigated. In section 4, vorticity balance in the frontal region, which may give better understanding of the flow field, is presented. Conclusions are given in the final section.

2. Model output, observational data, and methodology

a. Model output

In this study, we analyze outputs from a high-resolution CGCM, Community Earth System Model

(CESM; Hurrell et al. 2013; Small et al. 2014), developed by the National Center for Atmospheric Research (NCAR). It consists of the Community Atmosphere Model version 5 (CAM5; Neale et al. 2010) with the Community Land Model version 4 (Lawrence et al. 2011), and the Parallel Ocean Program version 2 (POP2; Smith et al. 2010) with the Community Ice Code version 4 (Hunke and Lipscomb 2008). The CAM5 is an atmospheric general circulation model (AGCM) with a horizontal resolution of about 0.25° and 30 vertical levels, while the POP2 model is an oceanic general circulation model (OGCM) with a horizontal resolution of 0.1° in a tripole grid with poles in North America and Asia and 62 vertical levels. These resolutions are sufficient to resolve air–sea interaction processes in midlatitude frontal regions. Since the drift in the global air temperature is detected in the first 50 years (Small et al. 2014), we use monthly mean outputs from the last 50 years of the 100-yr integration and daily mean outputs at the sea surface from the sixty-first to ninetieth year (daily mean data are available for these 30 years). To highlight the relatively large-scale SST front, all outputs are smoothed by a Gaussian filter with 50-km e-folding scale following Sugimoto et al. (2014), unless otherwise noted. As will be shown in section 3, the CESM has a relatively good skill in reproducing the SST front and MLD in the ARC region.

b. Observational data

For comparison with outputs from the CESM, we use monthly mean SST from Advanced Very High Resolution Radiometer (AVHRR) and Advanced Microwave Scanning Radiometer on the Earth Observing System (AMSR-E) Optimum Interpolation SST (AVHRR + AMSR OISST; Reynolds et al. 2007) on 0.25° longitude × 0.25° latitude grid, sea surface height (SSH) from Archiving, Validation and Interpretation of Satellite Oceanographic data (AVISO; Ducet et al. 2000) on 0.25° longitude × 0.25° latitude grid, and monthly surface heat fluxes from the Objectively Analyzed Air-Sea Fluxes (OAFlux; Yu and Weller 2007) on 1° longitude × 1° latitude grid. The analysis period is from January 2003 to December 2008, because spurious jumps in the intensity of the SST front in the ARC region are detected in AVHRR-only OISST (figure not shown). It may result from changes in the observation satellites (Reynolds et al. 2007; Masunaga et al. 2015) and/or clouds and aerosols around the midlatitude jet that hamper SST measurements (Chelton and Wentz 2005). Monthly temperature climatology is obtained from Monthly Isopycnal/Mixed-layer Ocean Climatology (MIMOC; Schmidtko et al. 2013) on 0.5° longitude × 0.5° latitude grid with 81 vertical levels, which is mainly based on the Argo float profiles in 2007–11.
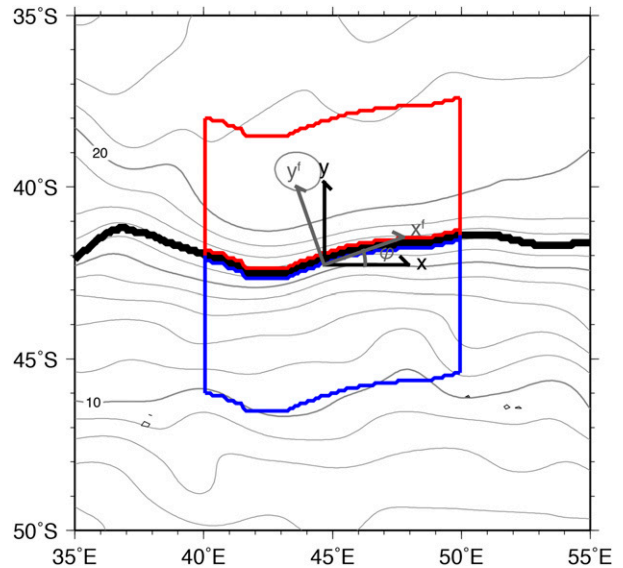

FIG. 2. The simulated SST front position (black) and MLT (gray contours) in January of the fifty-first integration year. A red (blue) box denotes the 10° longitude × 4° latitude averaging area on the northern (southern) side of the SST front. The black (gray) axis is the meridional–geographic (frontal) coordinate at one location. Thin (thick) contour intervals are 1 (5) °C.

c. Methodology

1) FRONTOGENESIS RATE EQUATION IN THE FRONTAL-COORDINATE SYSTEM

In this study, the frontal-coordinate system is adopted (Fig. 2). At each time step and each grid point, frontal-coordinate variables are estimated using a rotation matrix $\mathbf{A}$:

$$\mathbf{A} = \begin{pmatrix} \cos\varphi & \sin\varphi \\ -\sin\varphi & \cos\varphi \end{pmatrix}, \tag{1}$$

where φ is an angle of an isothermal line of mixed layer temperature (MLT) T_{mix} to the geographic coordinate (see the appendix). A variable with superscript f denotes the frontal-coordinate system, and x^f (y^f) represents the along-isotherm (cross-isotherm) coordinate.

The MLT balance equation in the frontal-coordinate system can be written as

$$\frac{\partial T_{\mathrm{mix}}}{\partial t} = \frac{Q_{\mathrm{net}} - q_{\mathrm{sw}}(-H)}{\rho_0 c_p H} - \mathbf{u}_{\mathrm{mix}}^f \cdot \nabla_h^f T_{\mathrm{mix}} - \frac{\Delta T}{H} w_e^f + (\mathrm{res}) \tag{2}$$

(e.g., Qiu and Kelly 1993; Moisan and Niiler 1998). Here, Q_{net} is the NHF, and $q_{\mathrm{sw}}(z)$ is downward shortwave radiation at depth z parameterized by

$$q_{sw}(z) = Q_{sw}\left[R\exp\left(\frac{z}{\gamma_1}\right) + (1-R)\exp\left(\frac{z}{\gamma_2}\right)\right] \quad (3)$$

(Paulson and Simpson 1977), where Q_{sw} is shortwave radiation at the sea surface, R ($=0.58$) is a separation constant, and γ_1 ($=0.35$ m) and γ_2 ($=23.0$ m) are attenuation length scales of Type I (clear water) from Jerlov (1976). Also, ρ_0 ($=1026$ kg m^{-3}) is the density of the seawater, c_p ($=3990$ J kg^{-1} °C^{-1}) is the specific heat of the seawater, H is the MLD defined as a depth at which the temperature is 0.5°C lower than the SST, $\mathbf{u}_{mix}^f$ is the frontal-coordinate horizontal velocity averaged within the mixed layer, $\nabla_h^f = (\partial/\partial x^f, \partial/\partial y^f)$ is the frontal-coordinate horizontal gradient operator, and $\Delta T \equiv T_{mix} - T_{-H-20m}$ is the temperature difference between the mixed layer and entrained water. Note that we use the temperature at 20 m below the base of the mixed layer as the temperature of the entrained water following Yasuda et al. (2000), Morioka et al. (2012), and Ohishi et al. (2016). The frontal-coordinate entrainment velocity w_e^f is represented by

$$w_e^f = \frac{\partial H}{\partial t} + \mathbf{u}^f(-H)\cdot\nabla_h^f H + w(-H), \quad (4)$$

where $\mathbf{u}^f(z)$ and $w(z)$ are horizontal velocity in the frontal-coordinate system and vertical velocity at depth z, respectively, and (res) includes the horizontal/vertical diffusion, the sheared stratified convergence term, and the terms associated with differentiation of the isothermal angle φ. Note that variables interpolated at 5-m intervals using the method of Akima (1970) are used for estimating variables associated with the MLD.

Meridional differentiation of Eq. (2) leads to the frontogenesis rate equation:

$$\frac{\partial}{\partial t}\left(\frac{\partial T_{mix}}{\partial y^*}\right) = \frac{\partial}{\partial y^*}\left[\frac{Q_{net} - q_{sw}(-H)}{\rho_0 c_p H}\right] - \frac{\partial}{\partial y^*}(\mathbf{u}_{mix}^f\cdot\nabla_h^f T_{mix})$$

$$- \frac{\partial}{\partial y^*}\left(\frac{\Delta T}{H}w_e^f\right) + (res) \quad (5)$$

(Tozuka and Cronin 2014; Ohishi et al. 2016). Here, to obtain the meridional derivative $\partial/\partial y^*$, the monthly climatologies are calculated by taking an area average over 10° longitude × 4° latitude on both sides of the SST front in 40°–50°E (Fig. 2), where the meridional position of the SST front is relatively stable (see section 3a), and their difference is taken. Note that, owing to the above method, the residual term [the last term on the RHS of Eq. (5)] includes the temporal and spatial covariance terms as well as the diffusion, shear, and isotherm angle derivative terms. We have confirmed that qualitatively the same results are obtained even if a slightly different extent was used.

2) VORTICITY BALANCE EQUATION IN THE FRONTAL-COORDINATE SYSTEM

To obtain better insight into along-/cross-isotherm velocity fields, the vorticity balance equation in the frontal-coordinate system is derived. As described in the appendix, the equation of motion in the frontal-coordinate system is

$$\frac{D\mathbf{u}^f}{Dt^f} + f\mathbf{k}\times\mathbf{u}^f = -\frac{1}{\rho_0}\nabla^f p + \frac{\partial}{\partial z}\left(\nu\frac{\partial\mathbf{u}^f}{\partial z}\right) + (res). \quad (6)$$

Here, $D/Dt^f = \partial/\partial t + \mathbf{v}^f\cdot\nabla^f$ is the material derivative in the frontal-coordinate system, where $\mathbf{v}^f$ and $\nabla^f = (\partial/\partial x^f, \partial/\partial y^f, \partial/\partial z)$ are the three-dimensional velocity and gradient operator in the frontal-coordinate system, respectively. Also, f is the vertical component of the Coriolis parameter, $\mathbf{k}$ is a unit vector in the vertical direction, p is the pressure, ν is a vertical turbulent viscosity parameter, and (res) includes the contributions from horizontal diffusion and differentiation of the isothermal angle φ. Taking the difference between the along-isotherm derivative of the cross-isotherm component and cross-isotherm derivative of the along-isotherm component of Eq. (6), that is, cross-differentiation of Eq. (6), leads to the vorticity equation in the frontal-coordinate system:

$$\frac{\partial\zeta^f}{\partial t} + \mathbf{u}^f\cdot\nabla_h^f\zeta^f + \beta(u^f\sin\varphi + v^f\cos\varphi)$$

$$= (f + \zeta^f)\frac{\partial w}{\partial z} + \frac{1}{\rho_0}\frac{\partial}{\partial z}\mathbf{k}\cdot[\nabla_h^f\times\boldsymbol{\tau}^f(z)]$$

$$- \mathbf{k}\cdot\nabla_h^f w\times\frac{\partial\mathbf{u}^f}{\partial z} + (res) \quad (7)$$

(cf. Williams et al. 2007; Delman et al. 2015), where $\zeta^f = \partial v^f/\partial x^f - \partial u^f/\partial y^f$ is the frontal-coordinate relative vorticity, $\beta = \partial f/\partial y$ is the planetary vorticity gradient, and $\boldsymbol{\tau}(z)$ is the stress vector at depth z represented by

$$\boldsymbol{\tau}(z) = \rho_0\nu\frac{\partial\mathbf{u}}{\partial z}. \quad (8)$$

By averaging Eq. (7) within the mixed layer, we obtain

$$\frac{\partial\zeta_{mix}^f}{\partial t} + \mathbf{u}_{mix}^f\cdot\nabla_h^f\zeta_{mix}^f + \beta(u_{mix}^f\sin\varphi + v_{mix}^f\cos\varphi) + \frac{\Delta\zeta^f}{H}w_e^f$$

$$= -f\frac{w(-H)}{H} + \frac{\mathbf{k}\cdot[\nabla_h^f\times\boldsymbol{\tau}^f(0)]}{\rho_0 H} + (res) \quad (9)$$

(cf. Moisan and Niiler 1998), where ζ_{mix}^f is the frontal-coordinate relative vorticity averaged within the mixed layer, $\Delta\zeta^f = \zeta_{mix}^f - \zeta_{-H}^f$ is the frontal-coordinate vorticity difference between the mixed layer and entrained water, and (res) includes the contribution from the horizontal diffusion, the vertical velocity except for the fourth term on the left-hand side (LHS) and the first term on the
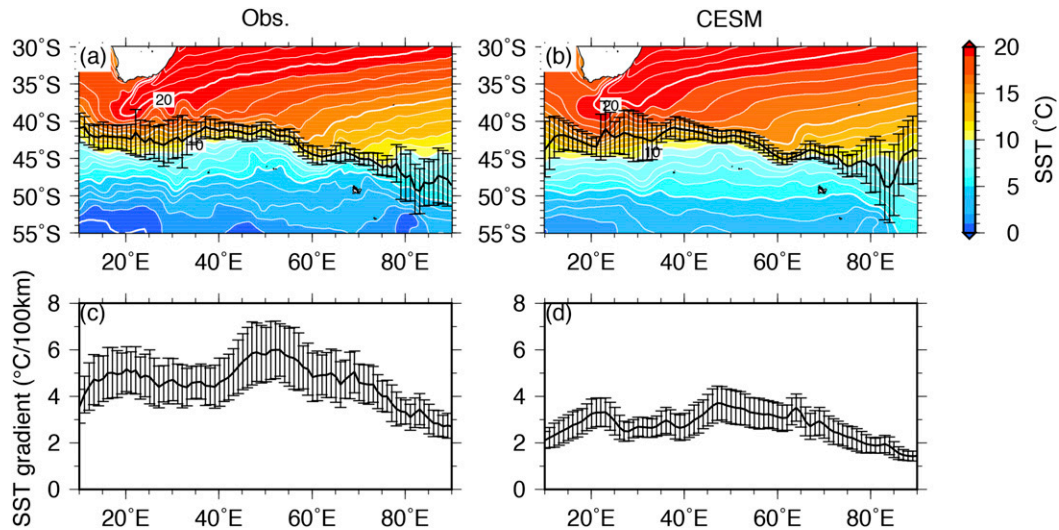
FIG. 3. Annual mean of the (a) observed and (b) simulated position of the SST front. Error bars denote the standard deviation over the analysis period. Color shading and white contours represent SST climatology. Thin (thick) contour intervals are 1 (5) °C. (c),(d) As in (a) and (b), but for the intensity of the SST front.

right-hand side (RHS) of Eq. (9), the stress curl at the mixed layer bottom, the shear, and the differentiation of the isothermal angle φ.

Since effects of eddy forcing on the time-mean flow field around midlatitude strong jets and western boundary currents are expected to be important, each variable X is decomposed as follows:

$$X = \overline{X} + \delta X, \tag{10}$$

where $\overline{X}$ and δX denote monthly climatology and a perturbation component, respectively (Hoskins 1983; Cronin 1996). Since $\partial \overline{X}/\partial t = \overline{\delta X} = 0$, temporal averaging of Eq. (9) leads to the frontal-coordinate time-mean vorticity balance equation averaged within the mixed layer:

$$\overline{v_{\mathrm{mix}}^f} = \left(\beta \, \overline{\cos \varphi} + \overline{\frac{\partial \zeta_{\mathrm{mix}}^f}{\partial y^f}} \right)^{-1} \left\{ -\overline{\left(\beta \delta \cos \varphi + \delta \frac{\partial \zeta_{\mathrm{mix}}^f}{\partial y^f} \right) \delta v_{\mathrm{mix}}^f} - \overline{\left(\beta \sin \varphi + \frac{\partial \zeta_{\mathrm{mix}}^f}{\partial x^f} \right) u_{\mathrm{mix}}^f} - \overline{\frac{\Delta \zeta^f}{H} w_e^f} \right.$$
$$\left. - f \overline{\frac{w(-H)}{H}} + \overline{\frac{\mathbf{k} \cdot [\nabla_h^f \times \boldsymbol{\tau}^f(0)]}{\rho_0 H}} \right\} + (\mathrm{res}). \tag{11}$$

This equation represents the vorticity balance between vorticity advections by a mean cross-isotherm flow, cross-isotherm eddy–mean interaction, and an along-isotherm flow; vorticity forcing by entrainment at the base of the mixed layer; vertical stretching owing to vertical velocity at the base of the mixed layer; vorticity forcing by the surface wind stress curl; and residual.

3. Observed and simulated frontogenesis/frontolysis in the ARC region

a. Comparison between characteristics of the observed and simulated SST fronts in the ARC region

To compare characteristics of the observed and simulated SST fronts in the ARC region, the intensity and position of the SST front are defined as the maximum of the horizontal SST gradient within 55°–35°S at each longitude and its latitude, respectively. Figure 3 shows their mean and standard deviation throughout the analysis period. The strong SST front with intensity of 2°–3°C (100 km)$^{-1}$ is simulated within 20°–70°E, although it is weaker compared to the observational intensity of 4°–5°C (100 km)$^{-1}$ partly because of the spatial low-pass filtering (Figs. 3c,d). The observed and simulated fronts are located in 45°–40°S and show relatively stable meridional position within 40°–70°E (Figs. 3a,b). To compare the seasonality in the observed and simulated SST fronts, the intensity is averaged within 40°–50°E, where the SST frontal position is relatively stable (Fig. 4). The observed (simulated) SST front has a maximum in June (a broad peak
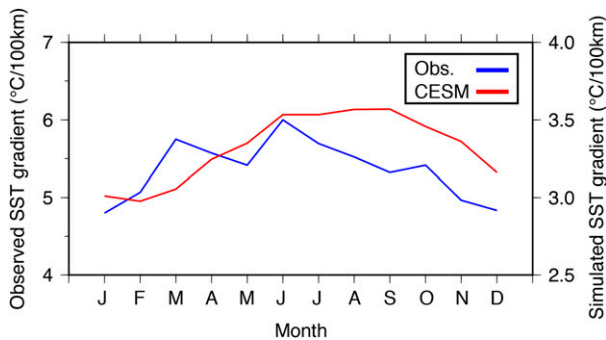
FIG. 4. Observed (blue) and simulated (red) monthly climatology of the intensity of the SST front averaged over 40°–50°E. The left (right) axis is for the observation (simulation).
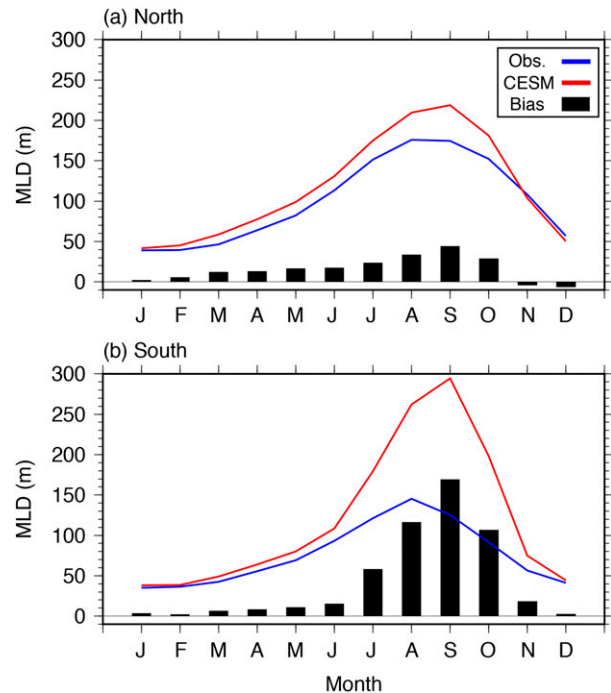

FIG. 5. (a) Observed (blue) and simulated (red) monthly climatology of the MLD in the northern region of the SST front. (b) As in (a), but for the southern region. Black bars indicate the monthly MLD bias.

in June–September) and a minimum in December (January–February). Although the phase is slightly shifted, the simulated SST front tends to be stronger (weaker) in austral winter (summer), consistent with the observation. Therefore, the main characteristics of the SST front in the ARC region are well simulated.

Since the MLD is a crucial factor for frontolysis by the NHF as pointed out in previous studies (Tozuka and Cronin 2014; Ohishi et al. 2016) and substantial MLD biases are known to exist in ocean reanalysis datasets (Toyoda et al. 2017) and CGCMs (Sallée et al. 2013; Ohishi et al. 2016), we validate the simulated MLD against the observation (Fig. 5). The simulated MLD is mostly consistent with the observation in the northern region (Fig. 5a), while it has relatively large biases greater than 50 m in the southern region during late austral winter (July–October) (Fig. 5b). However, their effects on frontolysis by the NHF seem to be small because of the seasonally deep MLD and small NHF during late austral winter, as described by Ohishi et al. (2016). Hence, we adopt the CESM with good skill in reproducing the SST front and MLD in the ARC region for investigating the detail of frontogenesis/frontolysis by oceanic processes.

b. Observed and simulated frontogenesis/frontolysis

The detailed mechanisms of frontogenesis/frontolysis are quantitatively investigated by estimating each term of Eq. (5) (Fig. 6). Here, the observed and simulated entrainment gradient terms [the third term on the RHS of Eq. (5)] are calculated only in March–August when the entrainment occurs in both northern and southern regions. Also, the observed entrainment velocity is assumed to be equal to the MLD tendency, because the simulated MLD tendency is dominant compared with the lateral induction and vertical velocity in both northern and southern regions (Fig. 7).

The observed and simulated first terms on the RHS of Eq. (5), called the NHF/MLD gradient term in this study, act as the dominant frontolysis throughout the

year (Fig. 6). As shown by Ohishi et al. (2016), the NHF strongly (weakly) relaxes the SST front in austral summer (winter) through mixed layer processes. On the other hand, for both observation and simulation, the sum of the horizontal advection gradient term [the second term on the RHS of Eq. (5)] and the residual term [the fourth term on the RHS of Eq. (5)] plays a major role in frontogenesis in all months and undergoes a distinct seasonal variation with stronger (weaker) frontogenesis in austral summer (winter) (Fig. 6). We note that it is estimated together as residual in the observation because of the lack of the sufficient number of velocity observations in the ocean interior. As shown in Fig. 6b, the simulated horizontal advection gradient term has the dominant contribution to frontogenesis throughout the year, and its seasonality corresponds well with the sum of the horizontal advection gradient and residual terms. The observed and simulated entrainment gradient terms [the third term on the RHS of Eq. (5)] have only minor contribution to frontogenesis/frontolysis in March–August. The simulated residual term moderately relaxes the front in all months, and this frontolysis process is comparable to the NHF/MLD gradient term in austral winter. Therefore, the frontogenesis by the horizontal advection approximately balances with the frontolysis by the NHF, and consequently the SST front is maintained throughout the year.
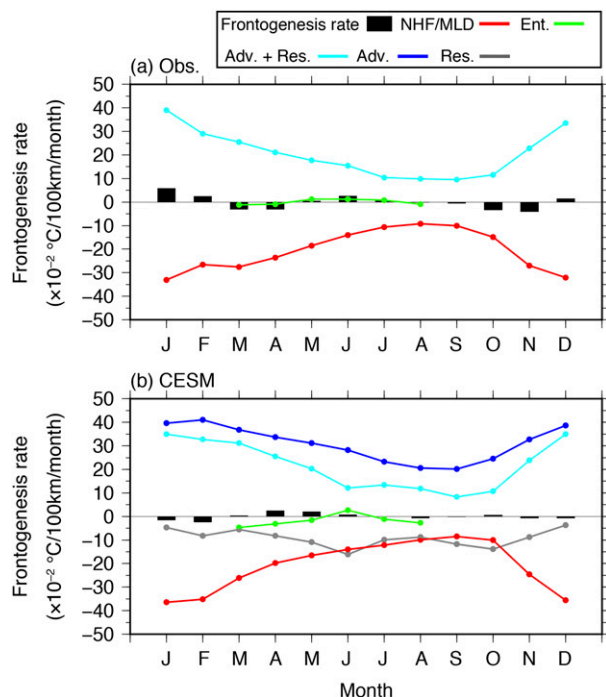
FIG. 6. (a) Observed and (b) simulated monthly climatology of the frontogenesis rate [LHS term of Eq. (5); black bar], the NHF/MLD gradient term [the first term on RHS of Eq. (5); red], the entrainment gradient term [the third term on the RHS of Eq. (5); green], and the sum of the horizontal advection gradient term [the second term on the RHS of Eq. (5)] and the residual term [the fourth term on the RHS of Eq. (5)] (cyan). In (b), the blue and gray lines represent the horizontal advection gradient and residual terms, respectively.

1) SIMULATED FRONTOGENESIS BY THE HORIZONTAL ADVECTION

To investigate the detailed mechanisms of the frontogenesis by the horizontal advection, we decompose the horizontal advection gradient term [the second term on the RHS of Eq. (5)] as

$$-\frac{\partial}{\partial y^*}(\mathbf{u}_{\text{mix}}^f \cdot \nabla_h^f T_{\text{mix}}) = -\frac{\partial v_{\text{mix}}^f}{\partial y^*}\frac{\partial T_{\text{mix}}}{\partial y^f} - v_{\text{mix}}^f\frac{\partial^2 T_{\text{mix}}}{\partial y^*\partial y^f}. \quad (12)$$

Because of the zero along-isotherm MLT gradient, only the cross-isotherm temperature advection can contribute to frontogenesis/frontolysis.

Figure 8a shows that the cross-isotherm confluence term [the first term on the RHS of Eq. (12)] has the dominant contribution to frontogenesis, while the cross-isotherm MLT gradient advection term [the second term on the RHS of Eq. (12)] is negligible. The cross-isotherm confluence term consists of two parts (i.e., the cross-isotherm convergence and MLT gradient). Since the cross-isotherm MLT gradient is large in the frontal region, the cross-isotherm confluence term acts as strong frontogenesis if there is cross-isotherm convergence. For this
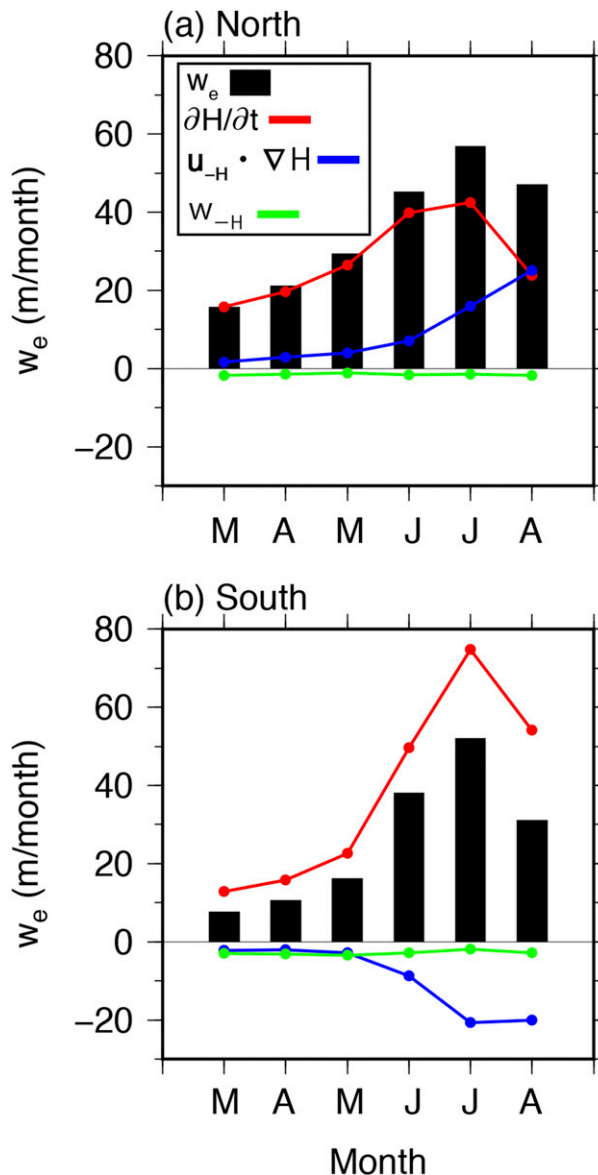

FIG. 7. Monthly climatology of each term in Eq. (4): the entrainment velocity (the LHS; black bar), MLD tendency (the first term on the RHS; red), lateral induction (the second term on the RHS; blue), and vertical velocity at the mixed layer bottom (the third term on the RHS; green) in the (a) northern and (b) southern regions in March–August when the entrainment occurs in both regions.

reason, the cross-isotherm velocity field is checked (Fig. 9). Although it is much weaker compared to the strong eastward along-isotherm current in the frontal region (Fig. 9a), the southward (northward) cross-isotherm confluent flow toward the SST front is distributed in a 4° latitudinal band north (the vast region south) of the front in 40°–60°E (Fig. 9b). This cross-isotherm confluence results in warmer (cooler) temperature advection toward the SST front on the northern (southern) side.
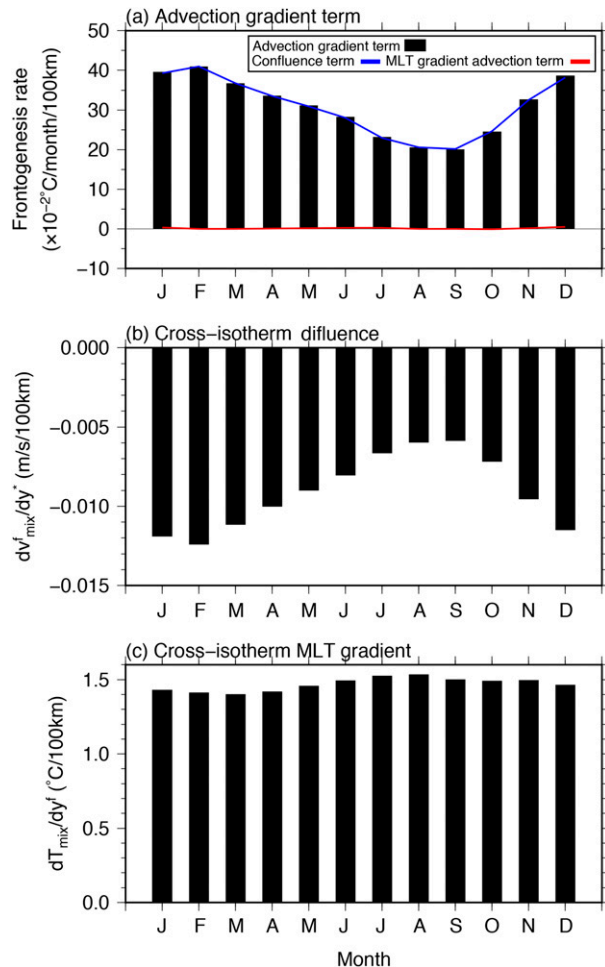
FIG. 8. Monthly climatology of (a) the horizontal advection gradient term [the LHS of Eq. (12); black bar], the cross-isotherm confluence term [the first term on the RHS of Eq. (12); blue], and the cross-isotherm MLT gradient advection term [the second term on the RHS of Eq. (12); red], (b) the cross-isotherm diffluence, and (c) the cross-isotherm MLT gradient averaged across the SST front in the northern and southern regions.

Furthermore, to see vertical structure of the cross-isotherm confluence, the mean along-/cross-isothermal flow and temperature fields in the upper 1500 m are examined using outputs from the CESM in the sixty-first to seventieth integration year and observational dataset, MIMOC (Fig. 10). Southward (northward) cross-isotherm flow north (south) of the front extends deeper than 1000-m depth (Fig. 10a). Also, the horizontal temperature gradient is greater than 1°C (100 km)$^{-1}$ in the upper 1000 m for both observation and simulation (Figs. 10b,c). Therefore, from the surface to 1000-m depth, frontogenesis may be caused by the confluent flow toward the SST front.

To investigate the seasonality of the cross-isotherm confluence term, the cross-isotherm confluence and
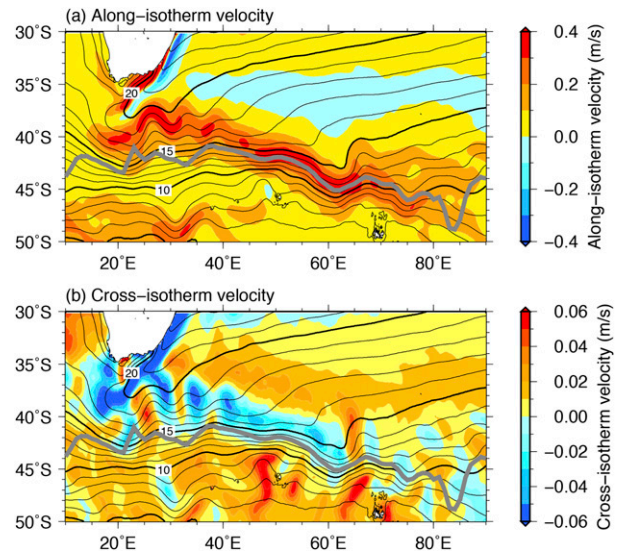

FIG. 9. Annual mean of (a) along-isotherm velocity u_{mix}^{f} and (b) cross-isotherm velocity v_{mix}^{f} averaged within the mixed layer. Black contours show MLT climatology and thin (thick) contour intervals are 1 (5) °C. The gray thick line represents the mean position of the SST front. Note that the color scales are different.

MLT gradient are examined in the ARC region. Figure 8b shows that the cross-isotherm confluence is stronger (weaker) in austral summer (winter), and its phase is consistent with the cross-isotherm confluence term. On the other hand, the cross-isotherm MLT gradient undergoes a very small seasonal variation with a slightly smaller (larger) gradient in austral summer (winter), and its phase is opposite to the cross-isotherm confluence term (Fig. 8c). Hence, the stronger (weaker) frontogenesis by the cross-isotherm confluence term in austral summer (winter) is attributed to the stronger (weaker) cross-isotherm confluence.

Since idealized model experiments suggested that the strength of the western boundary current is related to the confluent flow through the modification of the recirculation gyre (Waterman and Jayne 2011), the seasonality of the Agulhas Current, ARC, and ACC is examined. As shown in Fig. 11a, the southward Agulhas Current along the eastern coast of South Africa is stronger in austral summer compared to austral winter. Figure 11b shows that the ACC located around 50°S also undergoes a seasonal variation with the stronger (weaker) zonal current in austral summer (winter), although the seasonality of the ARC around 40°S is weak in 20°–30°E, where the retroflection and meandering occur (Figs. 1, 9). In 40°–50°E, where the ARC merges with the ACC, the stronger (weaker) zonal current is found in austral summer (winter) (Fig. 11c). Thus, the cross-isotherm confluence and currents associated with the Agulhas Current, ACC, and ARC are stronger
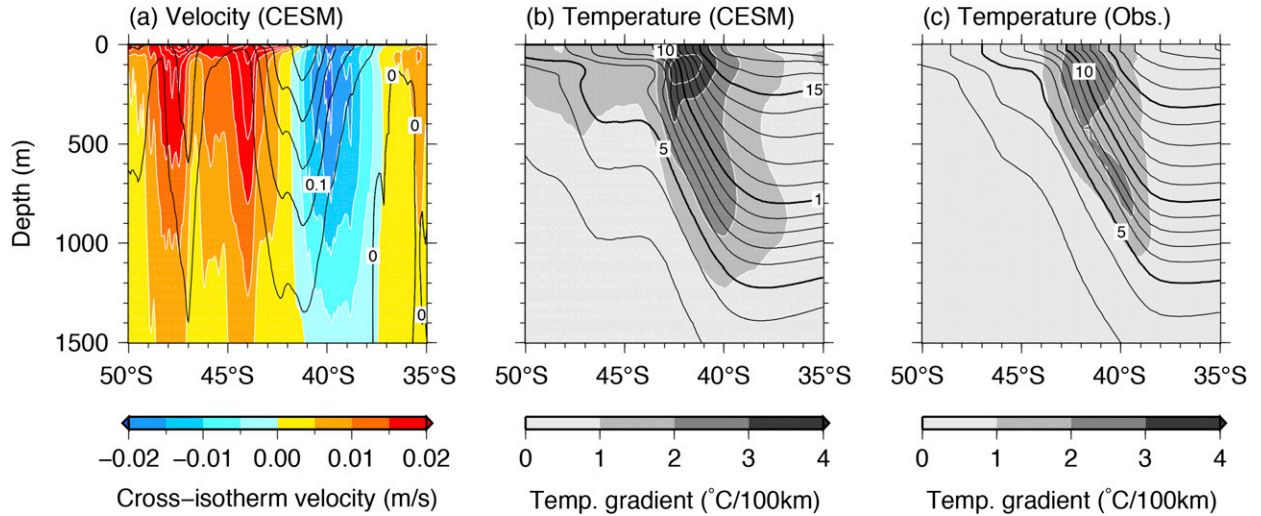
FIG. 10. Annual mean of (a) the simulated cross-isotherm (color shading and white contour) and along-isotherm velocity (black contour) and the (b) simulated and (c) observed horizontal temperature gradient (shading and white contour) and temperature (black contour) averaged over 40°–50°E. In (a), white (black) contour intervals are 0.005 (0.05) m s^{-1}. In (b) and (c), white contour intervals are 1°C (100 km)$^{-1}$, and thin (thick) black contour intervals are 1 (5) °C. Note that outputs from a high-resolution CGCM (CESM) without spatial low-pass filtering in the sixty-first to seventieth integration year are used in (a) and (b), and MIMOC is used in (c).

(weaker) in austral summer (winter), and this relationship is consistent with the previous study based on idealized models (Waterman and Jayne 2011).

2) OBSERVED AND SIMULATED FRONTOGENESIS/ FRONTOLYSIS BY THE ENTRAINMENT

Although the entrainment plays a relatively minor role in frontogenesis/frontolysis, its contribution is examined for more comprehensive understanding (Fig. 6). We decompose the entrainment gradient term [the third term on the RHS of Eq. (5)] as

$$-\frac{\partial}{\partial y*}\left(\frac{\Delta T}{H}w_e^f\right) = -\frac{\Delta T}{H}\frac{\partial w_e^f}{\partial y*} + \frac{\Delta T w_e^f}{H^2}\frac{\partial H}{\partial y*}$$
$$-\frac{w_e^f}{H}\frac{\partial \Delta T}{\partial y*}. \qquad (13)$$

Since relatively large MLD biases are detected south of the front in July–October, we only discuss frontogenesis/ frontolysis by the entrainment in March–May (Fig. 5b). As described by Ohishi et al. (2016), the SST front causes larger (smaller) latent heat release north (south)
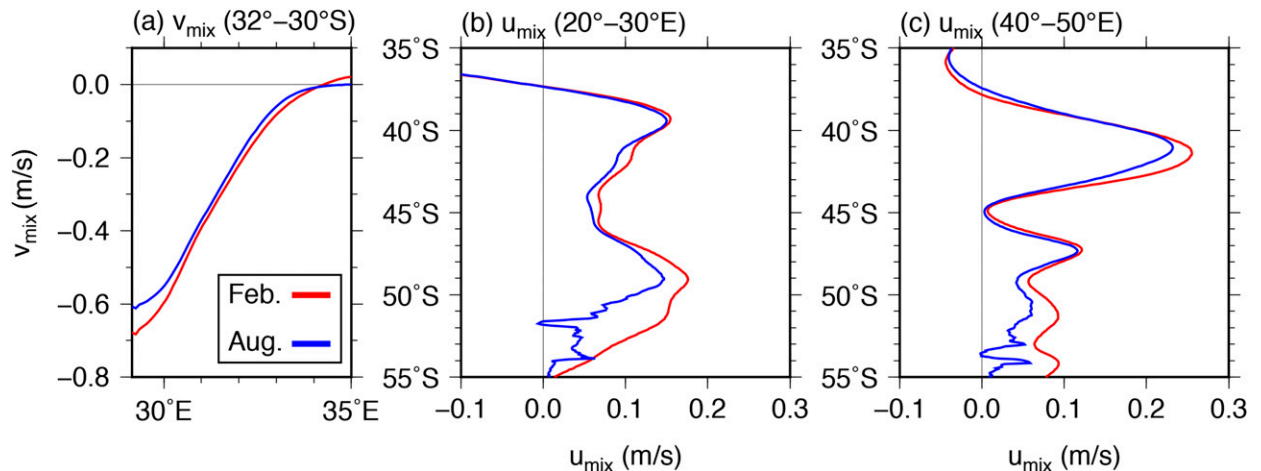

FIG. 11. (a) Zonal section of meridional velocity averaged within the mixed layer v_{mix} in 32°–30°S. Meridional section of zonal velocity averaged within the mixed layer u_{mix} in (b) 20°–30°E and (c) 40°–50°E. The red (blue) line represents monthly mean in February (August) when the cross-isotherm confluence in 40°–50°E is the strongest (weakest).
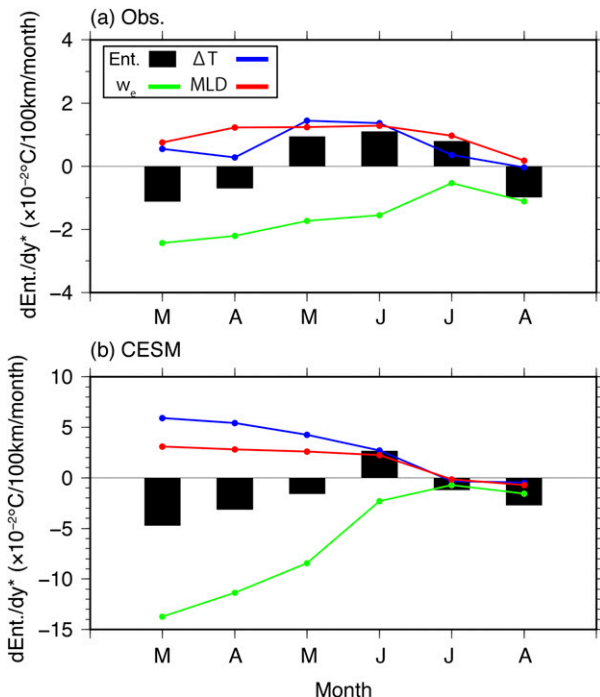
FIG. 12. Monthly climatology of each term in Eq. (13) for the (a) observation and (b) CESM: the entrainment gradient term (the LHS; black bar), the entrainment velocity gradient term (the first term on the RHS; green), the MLD gradient term (the second term on the RHS; red), and the temperature difference gradient term (the third term on the RHS; blue).

of the front by forming higher (lower) saturated specific humidity at the sea surface. The resulting stronger (weaker) surface cooling in the northern (southern) region mainly induces larger (smaller) entrainment velocity and thus forms a deeper (shallower) mixed layer. Larger (smaller) entrainment velocity on the northern (southern) side means that the mixed layer entrains a larger (smaller) amount of cold water from the lower layer, and therefore the observed and simulated entrainment velocity gradient terms [the first term on the RHS of Eq. (13)] tend to relax the SST front (Fig. 12).

In contrast, the observed and simulated MLD gradient terms [the second term on the RHS of Eq. (13)] act as frontogenesis. This is because the thicker (thinner) mixed layer north (south) of the front is less (more) sensitive to cooling by the entrainment. The observed and simulated temperature difference gradient terms [the third term on the RHS of Eq. (13)] also strengthen the SST front, because the entrainment weakly (strongly) cools the mixed layer owing to the smaller (larger) temperature difference between mixed layer and entrained water in the northern (southern) region. This temperature difference may be

linked to the Mode Water formation process (e.g., Hanawa and Talley 2001; Tsubouchi et al. 2010; Oka and Qiu 2012); a thicker vertically uniform layer is formed because of the wintertime deep mixed layer in the northern region.

Therefore, although the entrainment velocity gradient has a substantial contribution to frontolysis, it tends to be canceled out by frontogenesis caused by the MLD and temperature difference gradient. Consequently, the entrainment has a relatively small contribution to frontogenesis/frontolysis.

4. Vorticity balance

a. Vorticity balance associated with the cross-isotherm flow

Vorticity balance in the frontal-coordinate system can provide useful insight into the along-/cross-isotherm velocity field in the ARC region. Monthly climatology of each term in Eq. (11) is calculated using monthly outputs, because submonthly covariance terms estimated using daily outputs at the sea surface are small (figure not shown). Therefore, perturbation components are calculated as the difference between monthly outputs and monthly climatologies in this study.

The sum of the first to fifth terms on the RHS of Eq. (11) is negative (positive) north (south) of the front, in accord with the mean cross-isotherm velocity field [the LHS of Eq. (11)] (Figs. 13a,b). Although the residual term [the sixth term on the RHS of Eq. (11)] is not negligible, its spatial pattern is not consistent with the mean cross-isotherm velocity (Figs. 13a,c). Thus, we may assume that the first to fifth terms on the RHS of Eq. (11) are roughly in balance with the LHS term.

The spatial pattern of each of the first to fifth terms on the RHS of Eq. (11) is shown in Figs. 13d–h. The cross-isotherm eddy-mean vorticity interaction term [the first term on the RHS of Eq. (11)] has negative (positive) values in the northern (southern) region, corresponding well with the mean cross-isotherm velocity (Figs. 13a,d). However, its amplitude is slightly weaker compared to the cross-isotherm velocity. Hence, the cross-isotherm eddy-mean vorticity interaction term alone cannot completely balance with the cross-isotherm velocity. The along-isotherm vorticity advection term [the second term on the RHS of Eq. (11)] has substantial values, but its horizontal structure is patchy and not in agreement with the mean cross-isotherm velocity (Figs. 13a,e). The vorticity forcing by the entrainment [the third term on the RHS of Eq. (11)] is negligible (Fig. 13f), while the vertical
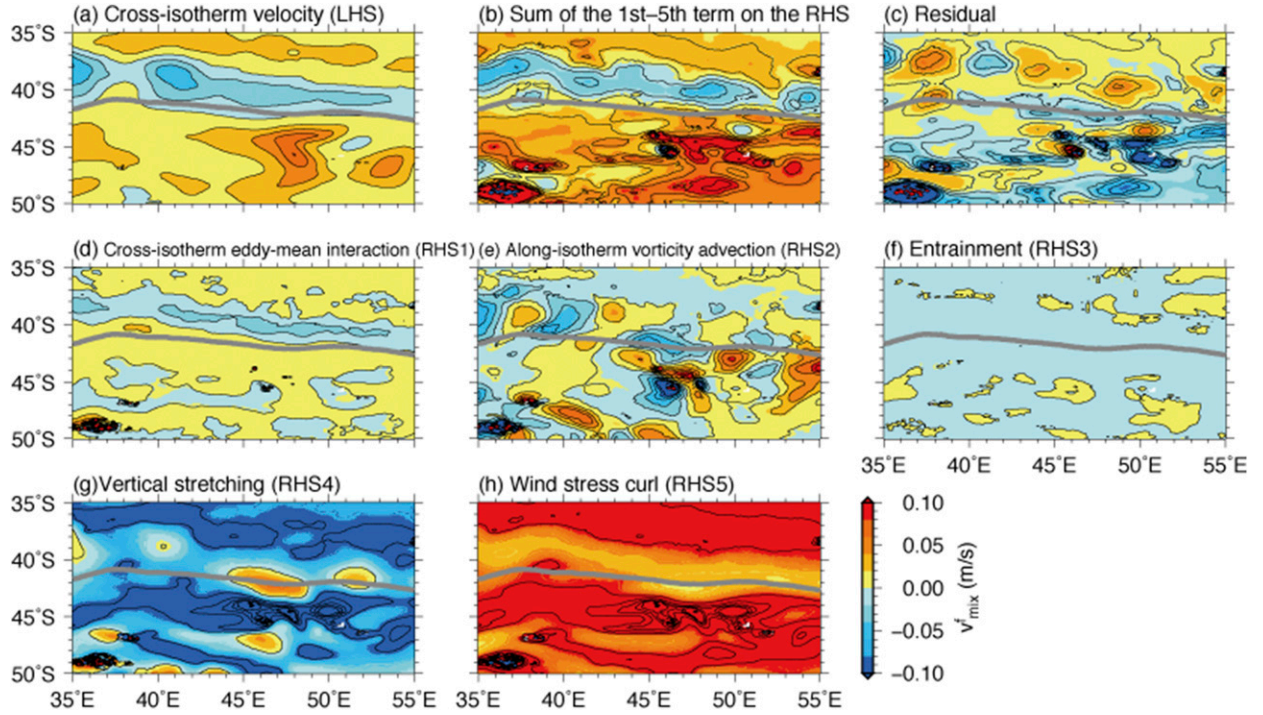
FIG. 13. Annual mean of (a) the cross-isotherm velocity [the LHS of Eq. (11)], (b) the sum of the first to fifth terms on the RHS of Eq. (11), (c) the residual term [the sixth term on the RHS of Eq. (11)], (d) the cross-isotherm eddy-mean vorticity interaction term [the first term on the RHS of Eq. (11)], (e) the along-isotherm vorticity advection term [the second term on the RHS of Eq. (11)], (f) the vorticity forcing by the entrainment [the third term on the RHS of Eq. (11)], (g) the vertical stretching term [the fourth term on the RHS of Eq. (11)], and (h) the vorticity forcing by the wind stress curl [the fifth term on the RHS of Eq. (11)]. Contour intervals are 0.02 m s^{-1} in (a)–(f) and 0.1 m s^{-1} in (g) and (h). The gray line represents the annual mean position of the SST front.

stretching term [the fourth term on the RHS of Eq. (11)] and the vorticity forcing by the wind stress curl [the fifth term on the RHS of Eq. (11)] are very large and have similar spatial patterns with smaller (larger) values in the northern (southern) region, except for the opposite sign (Figs. 13g,h).

b. Vorticity gradient balance related to the cross-isotherm confluence

To discuss quantitatively the vorticity balance related to the mean cross-isotherm confluent flow around the SST front, we calculate the meridional derivative of Eq. (11):

$$
\overline{\frac{\partial}{\partial y^*}}\overline{v_{\mathrm{mix}}^f} = \frac{1}{\beta\,\overline{\cos\varphi} + \overline{\partial\zeta_{\mathrm{mix}}^f/\partial y^f}}\,\overline{\frac{\partial}{\partial y^*}}\left\{ \underbrace{-\overline{\left(\beta\delta\cos\varphi + \delta\frac{\partial\zeta_{\mathrm{mix}}^f}{\partial y^f}\right)\delta v_{\mathrm{mix}}^f}}_{\text{1st term}} \underbrace{-\overline{\left(\beta\sin\varphi + \frac{\partial\zeta_{\mathrm{mix}}^f}{\partial x^f}\right)u_{\mathrm{mix}}^f}}_{\text{2nd term}} \underbrace{-\overline{\frac{\Delta\zeta^f}{H}w_e^f}}_{\text{3rd term}} \underbrace{-\overline{f\frac{w(-H)}{H}}}_{\text{4th term}} + \underbrace{\overline{\frac{\mathbf{k}\cdot[\nabla_h^f\times\boldsymbol{\tau}^f(0)]}{\rho_0 H}}}_{\text{5th term}} \right\}
$$

$$
\underbrace{-\frac{1}{(\beta\,\overline{\cos\varphi} + \overline{\partial\zeta_{\mathrm{mix}}^f/\partial y^f})^2}\left\{-\overline{\left(\beta\delta\cos\varphi + \delta\frac{\partial\zeta_{\mathrm{mix}}^f}{\partial y^f}\right)\delta v_{\mathrm{mix}}^f} - \overline{\left(\beta\sin\varphi + \frac{\partial\zeta_{\mathrm{mix}}^f}{\partial x^f}\right)u_{\mathrm{mix}}^f} - \overline{\frac{\Delta\zeta^f}{H}w_e^f} - \overline{f\frac{w(-H)}{H}} + \overline{\frac{\mathbf{k}\cdot[\nabla_h^f\times\boldsymbol{\tau}^f(0)]}{\rho_0 H}}\right\}\overline{\frac{\partial}{\partial y^*}}\left(\beta\,\overline{\cos\varphi} + \overline{\frac{\partial\zeta_{\mathrm{mix}}^f}{\partial y^f}}\right)}_{\text{6th term}}
$$

$$
\underbrace{+\ (\mathrm{res})}_{\text{7th term}}\ .
$$

(14)

Here, $\overline{\partial/\partial y^*}$ is calculated as the same method as $\partial/\partial y^*$, except for using monthly climatology of the SST front position. As shown in Fig. 14, the entrainment gradient

term [the third term on the RHS of Eq. (14)] and the meridional gradient of cross-isotherm vorticity gradient term [the sixth term on the RHS of Eq. (14)] play minor
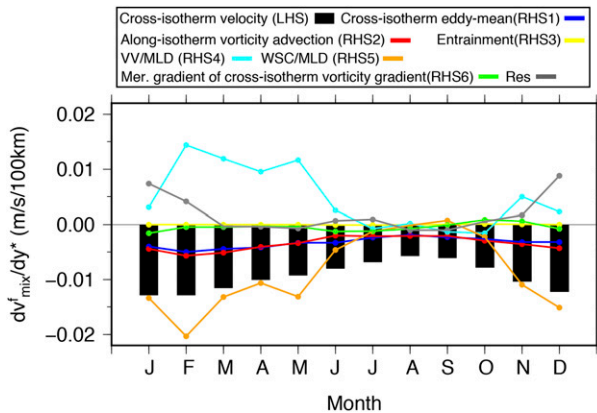
FIG. 14. Monthly climatology of each term in Eq. (14); the cross-isotherm velocity gradient term (the LHS; black bar), the cross-isotherm eddy-mean vorticity gradient term (the first term on the RHS; blue), the along-isotherm vorticity advection gradient term (the second term on the RHS; red), the entrainment gradient term (the third term on the RHS; yellow), the VV/MLD gradient term (the fourth term on the RHS; cyan), the WSC/MLD gradient term (the fifth term on the RHS; orange), the meridional gradient of cross-isotherm vorticity gradient term (the sixth term on the RHS; green), and the residual term (seventh term on the RHS; gray).
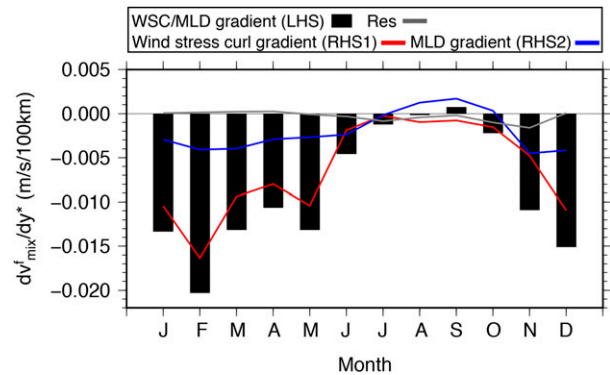

FIG. 15. Monthly climatology of each term in Eq. (15): the WSC/MLD gradient term (the LHS; black bar), the wind stress curl gradient term (the first term on the RHS; red), the MLD gradient term (the second term on the RHS; blue), and the residual term (the third term on the RHS; gray).

roles, while the cross-isotherm eddy-mean vorticity gradient term [the first term on the RHS of Eq. (14)] and the along-isotherm vorticity advection gradient term [the second term on the RHS of Eq. (14)] have substantial contributions in all months. Also, the fourth

term on the RHS of Eq. (14), referred to as the vertical velocity (VV)/MLD gradient term in this study, shows large negative values in February–May, while the fifth term on the RHS of Eq. (14), expressed as the wind stress curl (WSC)/MLD gradient term in this study, has large positive values in November–May.

1) CONTRIBUTIONS FROM WIND STRESS CURL AND VERTICAL VELOCITY TO VORTICITY FORCING

First, we investigate the detail of the WSC/MLD gradient term by decomposing it as follows:

$$\frac{1}{\beta \, \overline{\cos\varphi} + \overline{\partial \zeta_{\mathrm{mix}}^f / \partial y^f}} \overline{\frac{\partial}{\partial y^*} \left\{ \frac{\mathbf{k} \cdot [\nabla_h^f \times \boldsymbol{\tau}^f(0)]}{\rho_0 H} \right\}} = \frac{1}{\beta \, \overline{\cos\varphi} + \overline{\partial \zeta_{\mathrm{mix}}^f / \partial y^f}} \left\{ \frac{1}{\rho_0 \overline{H}} \overline{\frac{\partial}{\partial y^*} \mathbf{k} \cdot [\nabla_h^f \times \boldsymbol{\tau}^f(0)]} - \frac{\overline{\mathbf{k} \cdot [\nabla_h^f \times \boldsymbol{\tau}^f(0)]}}{\rho_0 \overline{H}^2} \overline{\frac{\partial}{\partial y^*} \overline{H}} \right\} + (\mathrm{res}), \quad (15)$$

where (res) includes high-order terms. Figure 15 shows that the wind stress curl gradient term [the first term on the RHS of Eq. (15)] is dominant, while the MLD gradient term [the second term on the RHS of Eq. (15)] and the residual term [the third term on the RHS of Eq. (15)] have minor contributions.

To seek the causes for the formation of the wind stress curl gradient term, the meridional profiles of the zonal wind stress and wind stress curl are plotted (Fig. 16). The westerly wind gradually weakens northward away from the core of the westerly jet located around 55°–50°S (Fig. 16a). However, the northward weakening of the westerly wind becomes locally small north of the SST front, and thus a minimum in the wind stress curl is formed around the SST front (Figs. 13h, 16b). This may be

explained by the vertical mixing mechanism (e.g., Wallace et al. 1989; Chelton et al. 2007; Takatama et al. 2012, 2015); over warmer (cooler) SSTs, since the static stability in the atmospheric boundary layer is lower (higher), the vertical turbulent mixing is strengthened (weakened), and thus the surface winds are accelerated (decelerated). Therefore, it is suggested that over the warmer (cooler) SSTs, the larger (smaller) wind stress occurs, and thus the minimum of the wind stress curl is formed above the SST front. Since the mean cross-isotherm vorticity gradient $\beta \, \overline{\cos\varphi} + \partial \zeta_{\mathrm{mix}}^f / \partial y^f$ is positive around the frontal region throughout the year (Fig. 17), the smaller (larger) positive wind stress curl on the warmer side induces smaller (larger) anticyclonic vorticity forcing and requires smaller (larger) cyclonic vorticity advection with a weaker
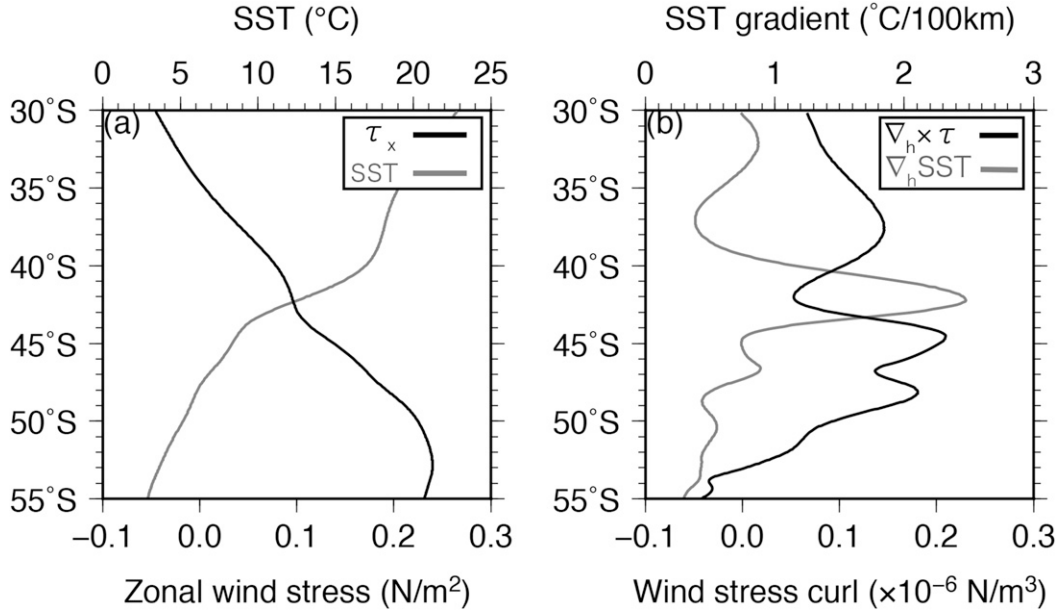
FIG. 16. Annual mean of (a) zonal wind stress (black) and SST (gray) and (b) wind stress curl (black) and SST gradient (gray) averaged over 40°–50°E.

(stronger) northward cross-isotherm flow, as expected from the Sverdrup relation (e.g., Sverdrup 1947).

At the same time, the wind stress curl can give rise to the vertical flow caused by the Ekman pumping:

$$w_{Ek} = \mathbf{k} \cdot \nabla_h^f \times \left[\frac{\boldsymbol{\tau}^f(0)}{\rho_0 f} \right]. \qquad (16)$$

Substitution of Eq. (16) into Eqs. (11) and (14) suggests that wind stress curl approximately cancels out the vertical velocity associated with the Ekman pumping except in austral summer (December–February) when the shallow mixed layer is very different from the Ekman layer depth (Fig. 5). In fact, the spatial pattern of the vertical stretching term corresponds well with the vorticity forcing by the wind stress curl (Figs. 13g,h). Additionally, as shown in Fig. 14, the VV/MLD gradient term [the fourth term on the RHS of Eq. (14)] almost cancels out the WSC/MLD gradient term [the fifth term on the RHS of Eq. (14)] except in austral summer. Therefore, although the contributions from the vertical velocity and wind stress curl gradient are large, they approximately cancel each other out especially in austral winter.

2) ALONG-/CROSS-ISOTHERM VORTICITY ADVECTION

The above results suggest that the cross-isotherm eddy-mean vorticity gradient term [the first term on the RHS of Eq. (14)] and the along-isotherm vorticity advection gradient term [the second term on the RHS of

Eq. (14)] are in balance with the mean cross-isotherm velocity gradient [the LHS of Eq. (14)] (Fig. 14). To understand how the cross-isotherm eddy-mean vorticity gradient term occurs, we display, as an example, monthly outputs in January of the seventy-seventh integration year when clear meandering is seen in the frontal region (Fig. 18). In 40°–50°E, an east–west oriented dipole structure of relative vorticity perturbations $\delta \zeta_{mix}^f$ is formed associated with the meandering (Fig. 18a). The anticyclonic relative vorticity perturbations on the western side lead to negative (positive) vorticity gradient perturbations $\beta \delta \cos \varphi + \delta(\partial \zeta_{mix}^f / \partial y^f)$ on the northern (southern) side of the flow from the crest to the trough (Fig. 18b). Also, southward cross-isotherm velocity perturbations δv_{mix}^f are distributed around the flow from the crest to the trough (Fig. 18c) and advect cyclonic (anticyclonic) relative vorticity

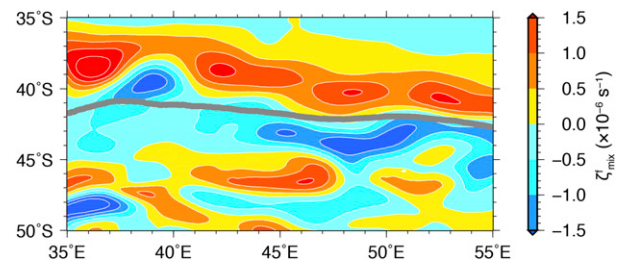FIG. 17. Annual mean of frontal-coordinate relative vorticity averaged over the mixed layer ζ_{mix}^f. Contour intervals are $0.5 \times 10^{-6} \text{ s}^{-1}$. The gray line represents the annual mean position of the SST front.
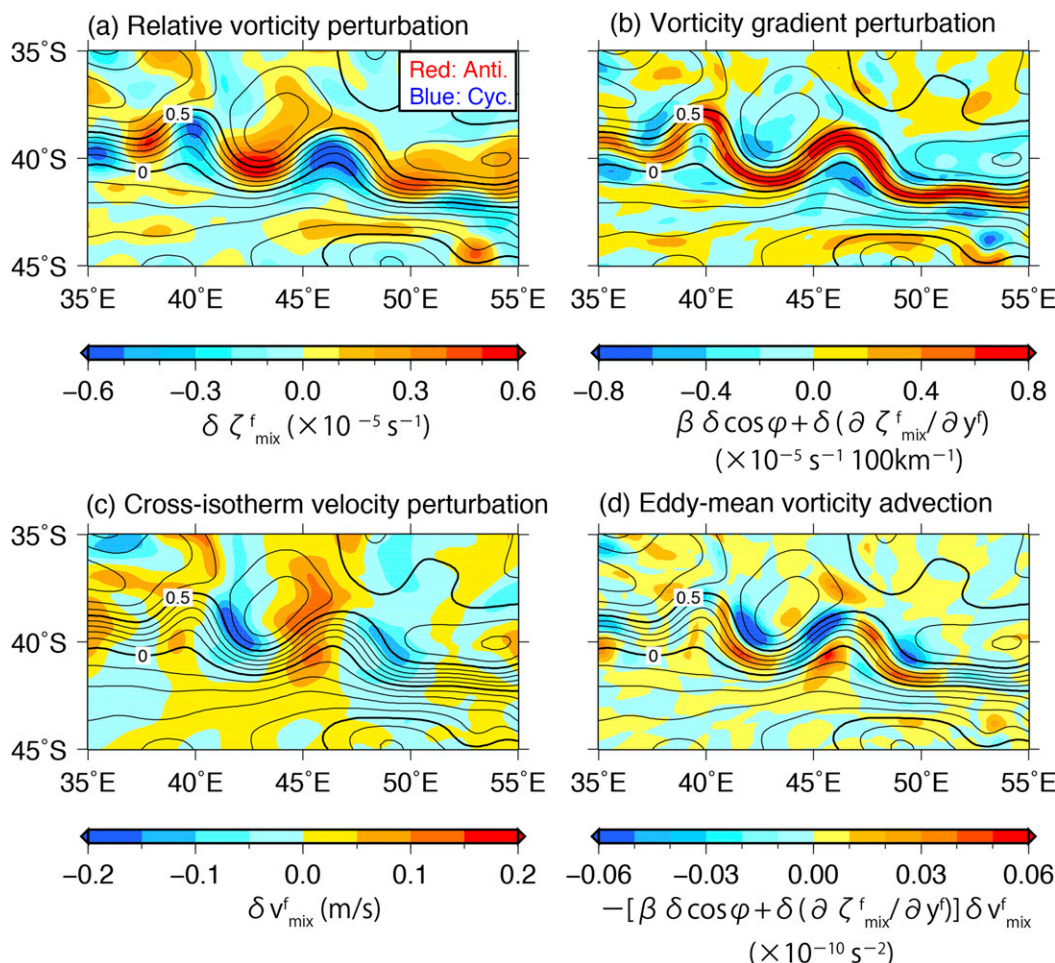
FIG. 18. Perturbation of (a) relative vorticity $\delta\zeta^f_{\text{mix}}$, (b) vorticity gradient $\beta\delta\cos\varphi + \delta(\partial\zeta^f_{\text{mix}}/\partial y^f)$, (c) cross-isotherm velocity δv^f_{mix}, and (d) vorticity advection by cross-isotherm eddy–mean interaction $-[\beta\delta\cos\varphi + \delta(\partial\zeta^f_{\text{mix}}/\partial y^f)]\delta v^f_{\text{mix}}$ in January of the seventy-seventh integration year. Contours represent SSH. Thin (thick) contour intervals are 0.1 (0.5) m. In (d), values multiplied by −1 are shown for easier comparison with the mean cross-isotherm vorticity advection.

perturbations in the northern (southern) region of the flow from the crest to the trough [Figs. 18d, 20a (shown below)]. On the eastern side with the cyclonic vorticity perturbations, similar structure is found; around the flow from the trough to the crest, the northward velocity perturbations advect cyclonic (anticyclonic) relative vorticity perturbations on the northern (southern) side (Figs. 18, 20a). Consequently, the eddy–mean interaction leads to the cyclonic (anticyclonic) vorticity advection in the northern (southern) region, which can be in balance

with the anticyclonic (cyclonic) vorticity advection by the southward (northward) mean cross-isotherm flow. Similar structure with the cross-isotherm eddy–mean interaction is seen in other months in the frontal region. The above vorticity advection by the cross-isotherm eddy–mean interaction balances with the half of that by the mean cross-isotherm confluence (Fig. 14).

Next, the detail of the along-isotherm vorticity advection gradient term [the second term on the RHS of Eq. (14)] is investigated by the following decomposition:

$$-\frac{1}{\beta\,\overline{\cos\varphi} + \overline{\partial\zeta^f_{\text{mix}}/\partial y^f}}\overline{\frac{\partial}{\partial y^*}\left[\left(\beta\sin\varphi + \frac{\partial\zeta^f_{\text{mix}}}{\partial x^f}\right)u^f_{\text{mix}}\right]} = -\frac{1}{\beta\,\overline{\cos\varphi} + \overline{\partial\zeta^f_{\text{mix}}/\partial y^f}}\left[\overline{u^f_{\text{mix}}}\,\overline{\frac{\partial}{\partial y^*}}\left(\beta\,\overline{\sin\varphi} + \overline{\frac{\partial\zeta^f_{\text{mix}}}{\partial x^f}}\right)\right.$$

$$\left.+\left(\beta\,\overline{\sin\varphi} + \overline{\frac{\partial\zeta^f_{\text{mix}}}{\partial x^f}}\right)\overline{\frac{\partial}{\partial y^*}\,u^f_{\text{mix}}}\right] + (\text{res}),\qquad(17)$$
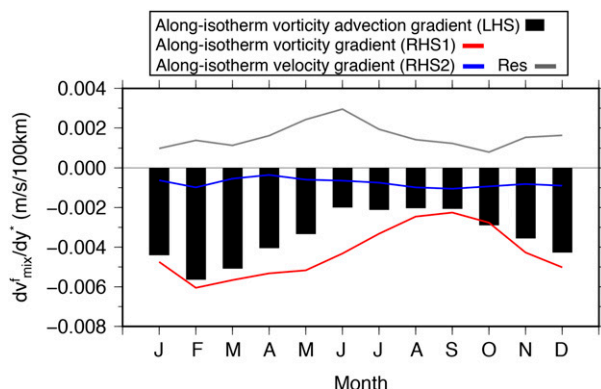
FIG. 19. Monthly climatology of each term in Eq. (17): the along-isotherm vorticity advection gradient term (the LHS; black bar), the contribution from the meridional gradient of along-isotherm vorticity gradient (the first term on the RHS; red), the mean along-isotherm velocity gradient term (the second term on the RHS; blue), and the residual term (the third term on the RHS; gray).

where (res) includes high-order terms. Figure 19 shows that the contribution from the meridional gradient of the mean along-isotherm vorticity gradient [the first term on the RHS of Eq. (17)] plays a major role, while the mean along-isotherm velocity gradient term [the second term on the RHS of Eq. (17)] and the residual term [the third term on the RHS of Eq. (17)] have relatively minor contributions. As shown in Fig. 17, the relative vorticity field has a meridionally asymmetric spatial pattern in the frontal region; the along-isotherm relative vorticity gradient averaged over 40°–50°E north of the front is less than $0.5 \times 10^{-6} \text{ s}^{-1} (100 \text{ km})^{-1}$, while that south of the front is almost $-2.0 \times 10^{-6} \text{ s}^{-1} (100 \text{ km})^{-1}$ throughout

the year. Therefore, owing to the strong eastward along-isotherm current in the frontal region, the mean along-isotherm positive (negative) vorticity gradient on the northern (southern) side results in small cyclonic (large anticyclonic) vorticity advection, which can be in balance with the anticyclonic (cyclonic) vorticity advection by the southward (northward) mean cross-isotherm flow.

Numerical experiments using a one-layer idealized model with a rectangular domain and flat bottom, which incorporates a flow with potential to cause barotropic instability at the western boundary, simulate meridionally symmetric recirculation (Waterman and Jayne 2011; Waterman and Hoskins 2013). This implies that the meridionally asymmetric pattern of the relative vorticity may be related to the contribution from realistic factors, such as the topographic effects, a more complicated horizontal flow field associated with the ARC and ACC, and ocean interior structure. The above vorticity advection gradient by the mean along-isotherm flow results from the meridional asymmetry of the relative vorticity (Figs. 17, 19, 20b) and balances with the half of vorticity advection gradient by the mean cross-isotherm confluence (Fig. 14).

5. Conclusions

In this study, using outputs from a high-resolution CGCM, the CESM, we have investigated the detailed mechanisms of frontogenesis/frontolysis by oceanic processes in the ARC region. The CESM has relatively good skill in reproducing the main features of the SST front in the ARC region such as intensity, position, and
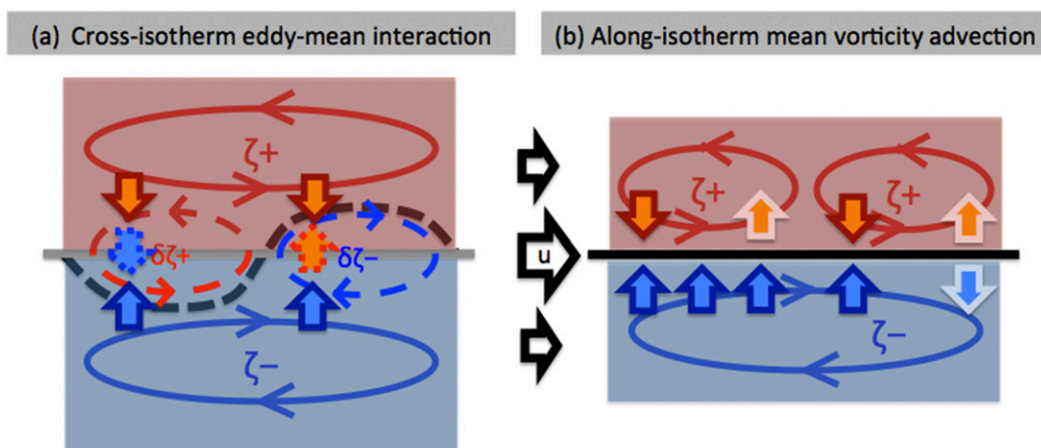

FIG. 20. Schematic diagrams of vorticity balances of the vorticity advection by the cross-isotherm confluence flow with that by (a) the cross-isotherm eddy–mean interaction and (b) the mean along-isotherm flow. The dashed (solid) line represents perturbation (mean) components: the black dashed (solid) line denotes the instantaneous (mean) frontal position (cf. Fig. 18); the red and blue dashed (solid) line indicates anomalous (mean) anticyclonic and cyclonic relative vorticity, respectively (cf. Figs. 17, 18a); and the dashed (solid) arrows indicate anomalous (mean) velocity (cf. Figs. 18c,d).
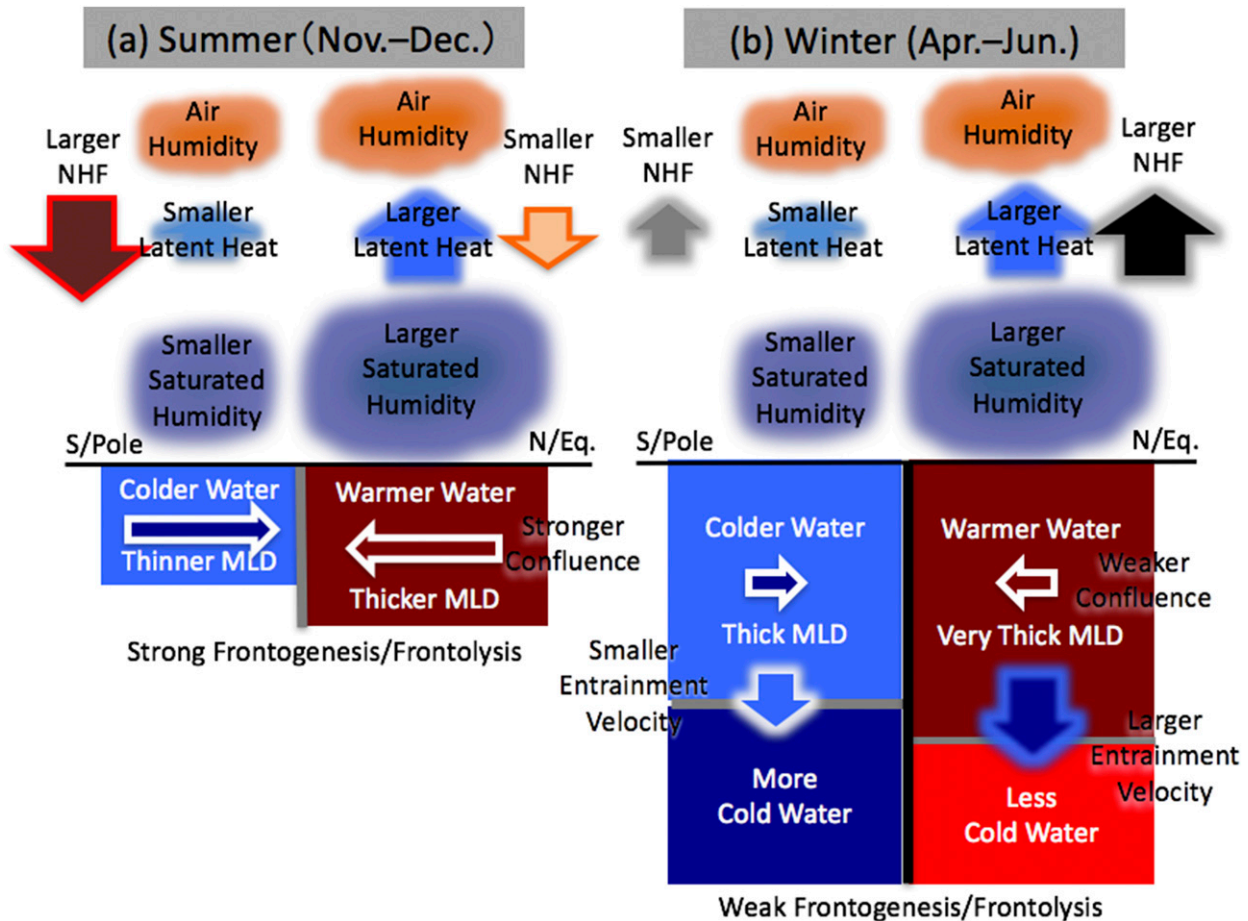
FIG. 21. Schematic diagrams of frontogenesis/frontolysis by the NHF, horizontal advection, and entrainment in austral (a) summer and (b) winter. Note that Fig. 16 by Ohishi et al. (2016) is modified. In (a) and (b), the dark red (light blue) box represents warmer (cooler) mixed layer, the dark red (dark blue) arrow in the box indicates southward (northward) cross-isotherm flows, and the cyan (light cyan) arrow denotes larger (smaller) latent heat release on the equatorward (poleward) side of the front. The red (orange) arrow in (a) denotes stronger (weaker) surface heating, while in (b) the black (gray) arrow represents stronger (weaker) surface cooling, the blue (cyan) arrow denotes larger (smaller) entrainment velocity, and the light red (dark blue) box indicates less (more) cold entrained water on the equatorward (poleward) side. The gray (black) vertical line between the boxes in (a) [(b)] represents a weaker (stronger) SST front.

seasonality (Figs. 3, 4). It also produces a realistic MLD in the frontal region (Fig. 5), which can play an important role in frontolysis by the NHF as shown in the previous studies (Tozuka and Cronin 2014; Ohishi et al. 2016).

In austral summer (winter), the simulated NHF strongly (weakly) relaxes the SST front as in the observation, while the simulated horizontal advection induces stronger (weaker) frontogenesis (Fig. 6). Although Ohishi et al. (2016) used the residual of the frontogenesis equation to quantify internal oceanic processes contributing to frontogenesis, this study is the first to reveal quantitatively that the horizontal advection is the dominant process for frontogenesis. In both observation and simulation, entrainment plays a minor role in frontogenesis/frontolysis. Thus, the SST front is

basically maintained by a balance between frontolysis by the NHF and frontogenesis by the horizontal advection. Figure 21 displays schematic diagrams summarizing the frontogenesis/frontolysis by the horizontal advection, NHF, and entrainment.

Cross-isotherm confluence in 40°–60°E plays the dominant role in the frontogenesis by the horizontal advection, because it induces the warmer (colder) water advection toward the SST front on the northern (southern) side (Figs. 8, 9, 21). This confluent flow is found in the upper 1000 m (Fig. 10). Also, the seasonality with stronger (weaker) frontogenesis in austral summer (winter) results from the stronger (weaker) cross-isotherm confluence, which may be linked to the strength of the Agulhas Current, ARC, and ACC (Figs. 11, 21). When vorticity balance was examined,

it was found that vorticity advection by the mean cross-isotherm confluence is in balance with that by the cross-isotherm eddy–mean interaction and the mean along-isotherm flow (Figs. 13, 14, 20).

As shown by a case study, southward cross-isotherm velocity perturbations related to the meandering advect cyclonic (anticyclonic) relative vorticity perturbations on the northern (southern) side of the flow from the crest to the trough (Figs. 18, 20a). Similar structure is found around the flow from the trough to the crest. As a result, cyclonic (anticyclonic) vorticity advection by the eddy–mean interaction occurs on the northern (southern) side and partly balances with the anticyclonic (cyclonic) vorticity advection by the mean cross-isotherm confluence. This north–south dipole pattern associated with the eddy–mean interaction is confirmed over the analysis period. Thus, it is suggested that the eddy forcing may play an important role in the dynamical balance associated with the mean cross-isotherm confluence.

Because of the meridional asymmetry of the relative vorticity and strong eastward along-isotherm current in the frontal region (Figs. 9, 17), small cyclonic (large anticyclonic) vorticity advection occurs on the northern (southern) side. Since the cyclonic (anticyclonic) vorticity advection requires anticyclonic (cyclonic) vorticity advection by a southward (northward) cross-isotherm flow, the resulting meridional gradient in vorticity advection by the along-isotherm flow partly balances with that by the cross-isotherm confluence (Fig. 20b).

Observed and simulated entrainment only acts as weak frontogenesis/frontolysis in austral fall and winter (Figs. 6, 12, 21b). This is because frontolysis by the entrainment velocity gradient, frontogenesis by the meridional gradient in the temperature difference between the mixed layer and entrained water, and frontogenesis by the MLD gradient tend to cancel each other out. As described by Ohishi et al. (2016), the SST gradient induces larger (smaller) latent heat release through the formation of larger (smaller) surface saturated specific humidity north (south) of the front. The resulting stronger (weaker) surface cooling on the northern (southern) side induces larger (smaller) entrainment velocity, and thus a thicker (thinner) mixed layer is formed. Since the larger (smaller) entrainment velocity on the northern (southern) side signifies that the mixed layer entrains a larger (smaller) amount of cold water from the lower layer, the meridional gradient in the entrainment velocity contributes to frontolysis. On the other hand, the MLD gradient acts as frontogenesis, because the thicker (thinner) mixed layer in the northern (southern) region is less (more) sensitive to cooling by the entrainment. Also, the temperature difference between the mixed layer and entrained water strengthens the SST front because of the entrainment of

less (more) cold water from the lower layer north (south) of the front. More vertically uniform temperature structure in the northern region may be related to the formation of the late-winter thick mixed layer, as proposed in the Mode Water formation process (e.g., Hanawa and Talley 2001; Tsubouchi et al. 2010; Oka and Qiu 2012).

Since the western boundary current along the eastern coast of the African continent transports warmer water from lower to higher latitudes (Figs. 1a, 9b), one may think that in western boundary current extension regions, the strong eastward along-isothermal current also induces temperature advection, and therefore it has a substantial contribution to frontogenesis. However, this is not true because of the zero along-isotherm thermal gradient. In fact, although the cross-isotherm confluent flow is much weaker compared to the along-isotherm flow, the cross-isotherm confluence plays an essential role in frontogenesis. This confluent flow was examined in terms of vorticity balance. Although the importance of the eddy–mean interaction for the cross-isotherm confluence is suggested, the causes of the confluent flow are not yet revealed, partly because the SST front was already established in the CGCM. In this regard, examining how an SST front develops from an initial state with a horizontally uniform temperature/salinity field using a high-resolution CGCM with a rectangular domain and flat bottom may provide better insight into frontogenesis.

Additionally, it was not possible to investigate how the residual term moderately relaxes the SST front in this study (Fig. 6b). To estimate the details of the residual term in the frontogenesis rate equation [the fourth term on the RHS of Eq. (5)], which includes horizontal/vertical diffusion, shear, isotherm angle derivative, and temporal and spatial covariance terms, we need to save all terms in the frontogenesis rate equation at each time step while integrating high-resolution CGCMs. It is important to reveal the contribution from the horizontal/vertical diffusion and eddy field. This is also a topic of future studies.

The methodology in this study can be applied to other SST fronts in western boundary currents, their extensions (e.g., Kelly et al. 2010), coastal regions (e.g., Chelton et al. 2007), and equatorial Pacific and Atlantic regions, where the sharp SST fronts accompanying tropical instability waves are observed north of the cold tongues in boreal summer (e.g., Düing et al. 1975; Legeckis 1977; Jochum et al. 2004; Willett et al. 2006). Furthermore, variations in SST fronts in the tropical Pacific with interannual time scale (e.g., Contreras 2002) and the Kuroshio Extension with decadal time scale (e.g., Qiu and Chen 2005) can be investigated quantitatively by applying the method in this study. Such studies may enhance the understanding of tropical and midlatitude air–sea interaction.

APPENDIX

Derivation of Equations in the Frontal-Coordinate System

For simplicity, the MLT balance and momentum equations in the frontal-coordinate system [Eqs. (2) and (6)] are derived on the assumption of no dependence of isotherm angle $\varphi(\mathbf{x}, t) = \varphi$. This assumption means that the residual terms in the frontal-coordinate equations [e.g., Eqs. (2) and (6)] actually include the terms with the temporal and spatial derivative of the isotherm angle φ. From the rotation matrix [Eq. (1)], the two-dimensional position in the frontal-coordinate system is

$$x^f = x\cos\varphi + y\sin\varphi, \quad \text{and} \quad (A1)$$

$$y^f = -x\sin\varphi + y\cos\varphi, \quad (A2)$$

as shown in Fig. 2. Equations (A1) and (A2) give

$$\frac{\partial}{\partial x} = \cos\varphi\frac{\partial}{\partial x^f} - \sin\varphi\frac{\partial}{\partial y^f}, \quad (A3)$$

$$\frac{\partial}{\partial y} = \sin\varphi\frac{\partial}{\partial x^f} + \cos\varphi\frac{\partial}{\partial y^f}, \quad (A4)$$

$$u = u^f\cos\varphi - v^f\sin\varphi, \quad \text{and} \quad (A5)$$

$$v = u^f\sin\varphi + v^f\cos\varphi. \quad (A6)$$

Using Eqs. (A3)–(A6), the advection term of a variable X can be represented as

$$-\mathbf{u}\cdot\nabla_h X = -\mathbf{u}^f\cdot\nabla_h^f X, \quad (A7)$$

where the $\mathbf{u}$ and ∇_h are the horizontal velocity and gradient operator in the geographic coordinate system, respectively. Therefore, the MLT balance equation in the frontal-coordinate system [Eq. (2)] can be obtained by applying Eq. (A7) to the geographic-coordinate equation.

The equation of motion in geographic coordinates is expressed as

$$\frac{D\mathbf{u}}{Dt} + f\mathbf{k}\times\mathbf{u} = -\frac{1}{\rho_0}\nabla p + \frac{\partial}{\partial z}\left(v\frac{\partial\mathbf{u}}{\partial z}\right) + (\text{res}), \quad (A8)$$

and its horizontal advection term can be represented as

$$u\frac{\partial u}{\partial x} + v\frac{\partial u}{\partial y} = \cos\varphi u^f\frac{\partial u^f}{\partial x^f} - \sin\varphi u^f\frac{\partial v^f}{\partial x^f}$$
$$+ \cos\varphi v^f\frac{\partial u^f}{\partial y^f} - \sin\varphi v^f\frac{\partial v^f}{\partial y^f}, \quad \text{and} \quad (A9)$$

$$u\frac{\partial v}{\partial x} + v\frac{\partial v}{\partial y} = \sin\varphi u^f\frac{\partial u^f}{\partial x^f} + \cos\varphi u^f\frac{\partial v^f}{\partial x^f}$$
$$+ \sin\varphi v^f\frac{\partial u^f}{\partial y^f} + \cos\varphi v^f\frac{\partial v^f}{\partial y^f}. \quad (A10)$$

Here, $D/Dt = \partial/\partial t + \mathbf{v}\cdot\nabla$ is the material derivative in the geographic coordinate system, where $\mathbf{v}$ and ∇ are the three-dimensional velocity and gradient operator in the geographic coordinate system, respectively. Using Eqs. (A9) and (A10), the frontal-coordinate momentum equation in an x^f direction (a y^f direction) [Eq. (6)] can be obtained by multiplying Eq. (A8) in an x-axis direction by $\cos\varphi$ ($-\sin\varphi$) and Eq. (A8) in a y-axis direction by $\sin\varphi$ ($\cos\varphi$) and then taking their sum.

REFERENCES

Akima, H., 1970: A new method of interpolation and smooth curve fitting based on local procedures. *J. Assoc. Comput. Mach.*, **17**, 589–602, doi:10.1145/321607.321609.

Beal, L. M., and Coauthors, 2011: On the role of the Agulhas system in ocean circulation and climate. *Nature*, **472**, 429–436, doi:10.1038/nature09983.

Boebel, O., T. Rossby, J. Lutjeharms, W. Zenk, and C. Barron, 2003: Path and variability of the Agulhas Return Current. *Deep-Sea Res. II*, **50**, 35–56, doi:10.1016/S0967-0645(02)00377-6.

Chelton, D. B., and F. J. Wentz, 2005: Global microwave satellite observations of sea surface temperature for numerical weather prediction and climate research. *Bull. Amer. Meteor. Soc.*, **86**, 1097–1115, doi:10.1175/BAMS-86-8-1097.

——, M. G. Schlax, and R. M. Samelson, 2007: Summertime coupling between sea surface temperature and wind stress in the California Current System. *J. Phys. Oceanogr.*, **37**, 495–517, doi:10.1175/JPO3025.1.

Contreras, R. F., 2002: Long-term observations of tropical instability waves. *J. Phys. Oceanogr.*, **32**, 2715–2722, doi:10.1175/1520-0485-32.9.2715.

Cronin, M., 1996: Eddy–mean flow interaction in the Gulf Stream at 68°W. Part II: Eddy forcing on the time-mean flow. *J. Phys. Oceanogr.*, **26**, 2132–2151, doi:10.1175/1520-0485(1996)026<2132:EMFIIT>2.0.CO;2.

——, and Coauthors, 2010: Monitoring ocean–atmosphere interactions in western boundary current extensions. *Proc. OceanObs'09: Sustained Ocean Observations and Information*

for Society Conf., Vol. 2, Venice, Italy, ESA, 20, doi:10.5270/OceanObs09.cwp.20.

Delman, A. S., J. L. McClean, J. Sprintall, L. D. Talley, E. Yulaeva, and S. R. Jayne, 2015: Effects of eddy vorticity forcing on the mean state of the Kuroshio Extension. *J. Phys. Oceanogr.*, **45**, 1356–1375, doi:10.1175/JPO-D-13-0259.1.

Ducet, N., P. Y. Le Traon, and G. Reverdin, 2000: Global high-resolution mapping of ocean circulation from TOPEX/Poseidon and ERS-1 and -2. *J. Geophys. Res.*, **105**, 19 477–19 498, doi:10.1029/2000JC900063.

Düing, W., and Coauthors, 1975: Meanders and long waves in the equatorial Atlantic. *Nature*, **257**, 280–284, doi:10.1038/257280a0.

Frankignoul, C., 1985: Sea surface temperature anomalies, planetary waves, and air–sea feedback in the middle latitudes. *Rev. Geophys.*, **23**, 357–390, doi:10.1029/RG023i004p00357.

Hanawa, K., and L. D. Talley, 2001: Mode waters. *Ocean Circulation and Climate: Observing and Modelling the Global Ocean*, G. Siedler, J. Church, and J. Gould, Eds., International Geophysics Series, Vol. 77, Academic Press, 373–386, doi:10.1016/S0074-6142(01)80129-7.

Hoskins, B. J., 1971: Atmospheric frontogenesis models: Some solutions. *Quart. J. Roy. Meteor. Soc.*, **97**, 139–153, doi:10.1002/qj.49709741202.

——, 1983: Modelling of the transient eddies and their feedback on the mean flow. *Large-Scale Dynamical Processes in the Atmosphere*, B. Hoskins and R. Pearce, Eds., Academic Press, 169–199.

——, and F. P. Bretherton, 1972: Atmospheric frontogenesis models: Mathematical formulation and solution. *J. Atmos. Sci.*, **29**, 11–37, doi:10.1175/1520-0469(1972)029<0011:AFMMFA>2.0.CO;2.

Hunke, E. C., and W. H. Lipscomb, 2008: CICE: The Los Alamos Sea Ice Model documentation and software user's manual version 4.0. Los Alamos National Laboratory Tech. Rep. LA-CC-06-012, 72 pp.

Hurrell, J. W., and Coauthors, 2013: The Community Earth System Model: A framework for collaborative research. *Bull. Amer. Meteor. Soc.*, **94**, 1339–1360, doi:10.1175/BAMS-D-12-00121.1.

Jerlov, N. G., 1976: *Marine Optics*. Elsevier, 230 pp.

Jochum, M., P. Malanotte-Rizzoli, and A. Busalacchi, 2004: Tropical instability waves in the Atlantic Ocean. *Ocean Modell.*, **7**, 145–163, doi:10.1016/S1463-5003(03)00042-8.

Kelly, K. A., R. J. Small, R. M. Samelson, B. Qiu, T. M. Joyce, Y. O. Kwon, and M. F. Cronin, 2010: Western boundary currents and frontal air–sea interaction: Gulf Stream and Kuroshio Extension. *J. Climate*, **23**, 5644–5667, doi:10.1175/2010JCLI3346.1.

Kushnir, Y., W. A. Robinson, I. Bladé, N. M. J. Hall, S. Peng, and R. Sutton, 2002: Atmospheric GCM response to extratropical SST anomalies: Synthesis and evaluation. *J. Climate*, **15**, 2233–2256, doi:10.1175/1520-0442(2002)015<2233:AGRTES>2.0.CO;2.

Kwon, Y.-O., M. A. Alexander, N. A. Bond, C. Frankignoul, H. Nakamura, B. Qiu, and L. Thompson, 2010: Role of the Gulf Stream and Kuroshio–Oyashio systems in large-scale atmosphere–ocean interaction: A review. *J. Climate*, **23**, 3249–3281, doi:10.1175/2010JCLI3343.1.

Lawrence, D. M., and Coauthors, 2011: Parameterization improvements and functional and structural advances in version 4 of the Community Land Model. *J. Adv. Model. Earth Syst.*, **3**, M03001, doi:10.1029/2011MS00045.

Legeckis, R., 1977: Long waves in the eastern equatorial Pacific Ocean: A view from a geostationary satellite. *Science*, **197**, 1179–1181, doi:10.1126/science.197.4309.1179.

Lutjeharms, J. R. E., 2006: *The Agulhas Current*. Springer, 329 pp.

——, and I. J. Ansorge, 2001: The Agulhas Return Current. *J. Mar. Syst.*, **30**, 115–138, doi:10.1016/S0924-7963(01)00041-0.

MacVean, M. K., and J. D. Woods, 1980: Redistribution of scalars during upper ocean frontogenesis: A numerical model. *Quart. J. Roy. Meteor. Soc.*, **106**, 293–311, doi:10.1002/qj.49710644805.

Masunaga, R., H. Nakamura, T. Miyasaka, K. Nishii, and Y. Tanimoto, 2015: Separation of climatological imprints of the Kuroshio Extension and Oyashio fronts on the wintertime atmospheric boundary layer: Their sensitivity to SST resolution prescribed for atmospheric reanalysis. *J. Climate*, **28**, 1764–1787, doi:10.1175/JCLI-D-14-00314.1.

Minobe, S., A. Kuwano-Yoshida, N. Komori, S.-P. Xie, and R. J. Small, 2008: Influence of the Gulf Stream on the troposphere. *Nature*, **452**, 206–209, doi:10.1038/nature06690.

——, M. Miyashita, A. Kuwano-Yoshida, H. Tokinaga, and S.-P. Xie, 2010: Atmospheric response to the Gulf Stream: Seasonal variations. *J. Climate*, **23**, 3699–3719, doi:10.1175/2010JCLI3359.1.

Moisan, J. R., and P. P. Niiler, 1998: The seasonal heat budget of the North Pacific: Net heat flux and heat storage rates (1950–1990). *J. Phys. Oceanogr.*, **28**, 401–421, doi:10.1175/1520-0485(1998)028<0401:TSHBOT>2.0.CO;2.

Morioka, Y., T. Tozuka, S. Masson, P. Terray, J.-J. Luo, and T. Yamagata, 2012: Subtropical dipole modes simulated in a coupled general circulation model. *J. Climate*, **25**, 4029–4047, doi:10.1175/JCLI-D-11-00396.1.

Nakamura, H., and A. Shimpo, 2004: Seasonal variations in the Southern Hemisphere storm tracks and jet streams as revealed in a reanalysis dataset. *J. Climate*, **17**, 1828–1844, doi:10.1175/1520-0442(2004)017<1828:SVITSH>2.0.CO;2.

——, T. Sampe, A. Goto, W. Ohfuchi, and S.-P. Xie, 2008: On the importance of midlatitude oceanic frontal zones for the mean state and dominant variability in the tropospheric circulation. *Geophys. Res. Lett.*, **35**, L15709, doi:10.1029/2008GL034010.

Neale, R. B., and Coauthors, 2010: Description of the NCAR Community Atmosphere Model (CAM 5.0). NCAR Tech. Note NCAR/TN-486-STR, 268 pp.

Nonaka, M., and S.-P. Xie, 2003: Covariations of sea surface temperature and wind over the Kuroshio and its extension: Evidence for ocean-to-atmosphere feedback. *J. Climate*, **16**, 1404–1413, doi:10.1175/1520-0442(2003)16<1404:COSSTA>2.0.CO;2.

——, H. Nakamura, B. Taguchi, N. Komori, A. Kuwano-Yoshida, and K. Takaya, 2009: Air–sea heat exchanges characteristic of a prominent midlatitude oceanic front in the south Indian Ocean as simulated in a high-resolution coupled GCM. *J. Climate*, **22**, 6515–6535, doi:10.1175/2009JCLI2960.1.

Ogawa, F., H. Nakamura, K. Nishii, T. Miyasaka, and A. Kuwano-Yoshida, 2012: Dependence of the climatological axial latitudes of the tropospheric westerlies and storm tracks on the latitude of an extratropical oceanic front. *Geophys. Res. Lett.*, **39**, L05804, https://doi.org/10.1029/2011GL049922.

Ohishi, S., T. Tozuka, and N. Komori, 2016: Frontolysis by surface heat flux in the Agulhas Return Current region with a focus on mixed layer processes: Observation and a high-resolution CGCM. *Climate Dyn.*, **47**, 3993–4007, doi:10.1007/s00382-016-3056-0.

Oka, E., and B. Qiu, 2012: Progress of North Pacific mode water research in the past decade. *J. Oceanogr.*, **68**, 5–20, doi:10.1007/s10872-011-0032-5.

O'Neill, L. W., D. B. Chelton, S. K. Esbensen, and F. J. Wentz, 2005: High-resolution satellite measurements of the atmospheric boundary layer response to SST variations along the Agulhas Return Current. *J. Climate*, **18**, 2706–2723, doi:10.1175/JCLI3415.1.

Paulson, C. A., and J. J. Simpson, 1977: Irradiance measurements in the upper ocean. *J. Phys. Oceanogr.*, **7**, 952–956, doi:10.1175/1520-0485(1977)007<0952:IMITUO>2.0.CO;2.

Pollard, R. T., and L. A. Regier, 1992: Vorticity and vertical circulation at an ocean front. *J. Phys. Oceanogr.*, **22**, 609–625, doi:10.1175/1520-0485(1992)022<0609:VAVCAA>2.0.CO;2.

Qiu, B., and K. A. Kelly, 1993: Upper-ocean heat balance in the Kuroshio Extension region. *J. Phys. Oceanogr.*, **23**, 2027–2041, doi:10.1175/1520-0485(1993)023<2027:UOHBIT>2.0.CO;2.

——, and S. Chen, 2005: Variability of the Kuroshio Extension jet, recirculation gyre, and mesoscale eddies on decadal time scales. *J. Phys. Oceanogr.*, **35**, 2090–2103, doi:10.1175/JPO2807.1.

Reynolds, R. W., T. M. Smith, C. Liu, D. B. Chelton, K. S. Casey, and M. G. Schlax, 2007: Daily high-resolution-blended analyses for sea surface temperature. *J. Climate*, **20**, 5473–5496, doi:10.1175/2007JCLI1824.1.

Rudnick, D. L., and R. E. Davis, 1988: Frontogenesis in mixed layers. *J. Phys. Oceanogr.*, **18**, 434–457, doi:10.1175/1520-0485(1988)018<0434:FIML>2.0.CO;2.

Sallée, J.-B., E. Shuckburgh, N. Bruneau, A. J. S. Meijers, T. J. Bracegirdle, and Z. Wang, 2013: Assessment of Southern Ocean mixed-layer depths in CMIP5 models: Historical bias and forcing response. *J. Geophys. Res. Oceans*, **118**, 1845–1862, doi:10.1002/jgrc.20157.

Samelson, R. M., 1993: Linear instability of a mixed-layer front. *J. Geophys. Res.*, **98**, 10 195–10 204, doi:10.1029/93JC00457.

——, and D. C. Chapman, 1995: Evolution of the instability of a mixed-layer front. *J. Geophys. Res.*, **100**, 6743–6759, doi:10.1029/94JC03216.

Schmidtko, S., G. C. Johnson, and J. M. Lyman, 2013: MIMOC: A global monthly isopycnal upper-ocean climatology with mixed layers. *J. Geophys. Res. Oceans*, **118**, 1658–1672, doi:10.1002/jgrc.20122.

Small, R. J., and Coauthors, 2014: A new synoptic scale resolving global climate simulation using the Community Earth System Model. *J. Adv. Model. Earth Syst.*, **6**, 1065–1094, doi:10.1002/2014MS000363.

Smith, R., and Coauthors, 2010: The Parallel Ocean Program (POP) reference manual. Los Alamos National Laboratory Tech. Rep. LAUR-10-01853, 141 pp.

Spall, M. A., 1995: Frontogenesis, subduction, and cross-front exchange at upper ocean fronts. *J. Geophys. Res.*, **100**, 2543–2557, doi:10.1029/94JC02860.

Sugimoto, S., N. Kobayashi, and K. Hanawa, 2014: Quasi-decadal variation in intensity of the western part of the winter subarctic SST front in the western North Pacific: The influence of Kuroshio Extension path state. *J. Phys. Oceanogr.*, **44**, 2753–2762, doi:10.1175/JPO-D-13-0265.1.

Sverdrup, H. U., 1947: Wind-driven currents in a baroclinic ocean; with application to the equatorial currents of the eastern Pacific. *Proc. Natl. Acad. Sci. USA*, **33**, 318–326, doi:10.1073/pnas.33.11.318.

Takatama, K., S. Minobe, M. Inatsu, and R. J. Small, 2012: Diagnostics for near-surface wind convergence/divergence response to the Gulf Stream in a regional atmospheric model. *Atmos. Sci. Lett.*, **13**, 16–21, doi:10.1002/asl.355.

——, ——, ——, and ——, 2015: Diagnostics for near-surface wind response to the Gulf Stream in a regional atmospheric model. *J. Climate*, **28**, 238–255, doi:10.1175/JCLI-D-13-00668.1.

Thompson, L., 2000: Ekman layers and two-dimensional frontogenesis in the upper ocean. *J. Geophys. Res.*, **105**, 6437–6451, doi:10.1029/1999JC900336.

Tokinaga, H., Y. Tanimoto, and S.-P. Xie, 2005: SST-induced surface wind variations over the Brazil–Malvinas confluence: Satellite and in situ observations. *J. Climate*, **18**, 3470–3482, doi:10.1175/JCLI3485.1.

——, ——, ——, T. Sampe, H. Tomita, and H. Ichikawa, 2009: Ocean frontal effects on the vertical development of clouds over the western North Pacific: In situ and satellite observations. *J. Climate*, **22**, 4241–4260, doi:10.1175/2009JCLI2763.1.

Toyoda, T., and Coauthors, 2017: Intercomparison and validation of the mixed layer depth fields of global ocean syntheses. *Climate Dyn.*, **49**, 753–773, doi:10.1007/s00382-015-2637-7.

Tozuka, T., and M. F. Cronin, 2014: Role of mixed layer depth in surface frontogenesis: The Agulhas Return Current front. *Geophys. Res. Lett.*, **41**, 2447–2453, doi:10.1002/2014GL059624.

Tsubouchi, T., T. Suga, and K. Hanawa, 2010: Indian Ocean Subtropical Mode Water: Its water characteristics and spatial distribution. *Ocean Sci.*, **6**, 41–50, doi:10.5194/os-6-41-2010.

Wallace, J. M., T. P. Mitchell, and C. Deser, 1989: The influence of sea-surface temperature on surface wind in the eastern equatorial Pacific: Seasonal and interannual variability. *J. Climate*, **2**, 1492–1499, https://doi.org/10.1175/1520-0442(1989)002<1492:TIOSST>2.0.CO;2.

Wang, D.-P., 1993: Model of frontogenesis: Subduction and upwelling. *J. Mar. Res.*, **51**, 497–513, doi:10.1357/0022240933224034.

Waterman, S., and S. R. Jayne, 2011: Eddy-mean flow interactions in the along-stream development of a western boundary current jet: An idealized model study. *J. Phys. Oceanogr.*, **41**, 682–707, doi:10.1175/2010JPO4477.1.

——, and B. J. Hoskins, 2013: Eddy shape, orientation, propagation, and mean flow feedback in western boundary current jets. *J. Phys. Oceanogr.*, **43**, 1666–1690, doi:10.1175/JPO-D-12-0152.1.

Weller, R. A., 1991: Overview of the Frontal Air-Sea Interaction Experiment (FASINEX): A study of air-sea interaction in a region of strong oceanic gradients. *J. Geophys. Res.*, **96**, 8501–8516, doi:10.1029/90JC01868.

Willett, C. S., R. R. Leben, and M. F. Lavín, 2006: Eddies and tropical instability waves in the eastern tropical Pacific: A review. *Prog. Oceanogr.*, **69**, 218–238, doi:10.1016/j.pocean.2006.03.010.

Williams, R. G., C. Wilson, and C. W. Hughes, 2007: Ocean and atmosphere storm tracks: The role of eddy vorticity forcing. *J. Phys. Oceanogr.*, **37**, 2267–2289, doi:10.1175/JPO3120.1.

Yasuda, I., T. Tozuka, M. Noto, and S. Kouketsu, 2000: Heat balance and regime shifts of the mixed layer in the Kuroshio Extension. *Prog. Oceanogr.*, **47**, 257–278, doi:10.1016/S0079-6611(00)00038-0.

Yu, L., and R. A. Weller, 2007: Objectively analyzed air–sea heat fluxes for the global ice-free oceans (1981–2005). *Bull. Amer. Meteor. Soc.*, **88**, 527–539, doi:10.1175/BAMS-88-4-527.